EUROPEAN ORGANIZATION FOR NUCLEAR RESEARCH (CERN)

CERN-PH-EP-2014-202
LHCb-PAPER-2014-041
12 August 2014

arXiv:1408.2748v2 [hep-ex] 22 Oct 2014

Measurement of the CKM angle γ using $B^{\pm} \to DK^{\pm}$ with $D \to K^0_S\pi^+\pi^-, K^0_S K^+ K^-$ decays

The LHCb collaboration[†]

Abstract

A binned Dalitz plot analysis of $B^{\pm} \to DK^{\pm}$ decays, with $D \to K^0_S\pi^+\pi^-$ and $D \to K^0_S K^+ K^-$, is performed to measure the *CP*-violating observables $x_{\pm}$ and $y_{\pm}$, which are sensitive to the Cabibbo-Kobayashi-Maskawa angle γ. The analysis exploits a sample of proton-proton collision data corresponding to $3.0\,\text{fb}^{-1}$ collected by the LHCb experiment. Measurements from CLEO-c of the variation of the strong-interaction phase of the D decay over the Dalitz plot are used as inputs. The values of the parameters are found to be $x_+ = (-7.7 \pm 2.4 \pm 1.0 \pm 0.4) \times 10^{-2}$, $x_- = (2.5 \pm 2.5 \pm 1.0 \pm 0.5) \times 10^{-2}$, $y_+ = (-2.2 \pm 2.5 \pm 0.4 \pm 1.0) \times 10^{-2}$, and $y_- = (7.5 \pm 2.9 \pm 0.5 \pm 1.4) \times 10^{-2}$. The first, second, and third uncertainties are the statistical, the experimental systematic, and that associated with the precision of the strong-phase parameters. These are the most precise measurements of these observables and correspond to $\gamma = (62^{+15}_{-14})^\circ$, with a second solution at $\gamma \to \gamma + 180^\circ$, and $r_B = 0.080^{+0.019}_{-0.021}$, where r_B is the ratio between the suppressed and favoured B decay amplitudes.

Published in JHEP 10 (2014) 097

© CERN on behalf of the LHCb collaboration, license CC-BY-4.0.

[†]Authors are listed at the end of this paper.

1 Introduction

A precise determination of the Cabibbo-Kobayashi-Maskawa (CKM) angle $\gamma \equiv \arg(-V_{\rm ud}V_{\rm ub}^*/V_{\rm cd}V_{\rm cb}^*)$ is of great value in testing the Standard Model (SM) description of *CP* violation. Measurements of this weak phase in tree-level processes involving the interference between $b \to c\bar{u}s$ and $b \to u\bar{c}s$ transitions are expected to be insensitive to contributions from physics beyond the SM. Such measurements therefore provide a SM benchmark against which other observables, more likely to be affected by physics beyond the SM, can be compared. The effects of the interference can be probed by studying *CP*-violating observables in $B^\pm \to DK^\pm$ decays, where D represents a neutral D meson reconstructed in a final state that is common to both D^0 and $\overline{D}^0$ decays. Examples of such final states recently studied by LHCb are two-body decays [1], multibody decays that are not self-conjugate [2, 3], and self-conjugate three-body decays, such as $K^0_{\rm S}\pi^+\pi^-$ and $K^0_{\rm S}K^+K^-$, designated collectively as $K^0_{\rm S}h^+h^-$ [4]. Similar measurements have also been made using neutral B^0 [5] and B^0_s [6] mesons.

Sensitivity to γ in $B^\pm \to DK^\pm$, $D \to K^0_{\rm S}h^+h^-$ decays is obtained by comparing the distribution of the events in the $D \to K^0_{\rm S}h^+h^-$ Dalitz plot for reconstructed B^+ and B^- mesons [7, 8]. Knowledge of the variation of the strong-interaction phase of the D decay over the Dalitz plot is required to determine γ. One approach, adopted by the BaBar [9–11], Belle [12–14] and LHCb [15] collaborations, is to use an amplitude model determined from flavour-tagged $D \to K^0_{\rm S}h^+h^-$ decays to provide this input. An attractive alternative [7, 16, 17] is to use direct measurements of the strong-phase variation over bins of the Dalitz plot, thereby avoiding model-related systematic uncertainties. Such measurements can be obtained using quantum-correlated $D^0\overline{D}^0$ pairs from $\psi(3770)$ decays and have been made at CLEO-c [18]. This model-independent method has been applied to measurements at Belle [19] using $B^\pm \to DK^\pm$, $D \to K^0_{\rm S}\pi^+\pi^-$ decays, and at LHCb [4] using a subset of data used in the current analysis.

In this paper, *pp* collision data at a centre-of-mass energy $\sqrt{s} = 7$ (8) TeV, accumulated by LHCb in 2011 (2012) and corresponding to a total integrated luminosity of $3.0\,{\rm fb}^{-1}$, are exploited to perform a model-independent study of the decay mode $B^\pm \to DK^\pm$ with $D \to K^0_{\rm S}\pi^+\pi^-$ and $D \to K^0_{\rm S}K^+K^-$. In addition to benefiting from a larger data set than that used in Ref. [4] the current study makes use of improved analysis techniques. The results presented here thus supersede those of Ref. [4].

2 Overview of the analysis

The amplitude of the decay $B^- \to DK^-$, $D \to K^0_{\rm S}h^+h^-$ can be written as a superposition of the $B^- \to D^0K^-$ and $B^- \to \overline{D}^0K^-$ contributions, given by

$$A_B(m^2_-, m^2_+) \propto A + r_B e^{i(\delta_B - \gamma)}\overline{A}. \tag{1}$$

Here m^2_- and m^2_+ are the invariant masses squared of the $K^0_{\rm S}h^-$ and $K^0_{\rm S}h^+$ combinations, respectively, that define the position of the decay in the Dalitz plot, $A = A(m^2_-, m^2_+)$ is

the $D^0 \to K^0_S h^+ h^-$ amplitude and $\overline{A} = \overline{A}(m^2_-, m^2_+)$ the $\overline{D}^0 \to K^0_S h^+ h^-$ amplitude. The parameters r_B and δ_B are the ratio of the magnitudes of the $B^- \to \overline{D}^0 K^-$ and $B^- \to D^0 K^-$ amplitudes, and the strong-phase difference between them. The equivalent expression for the charge-conjugated decay $B^+ \to DK^+$ is obtained by making the substitutions $\gamma \to -\gamma$ and $A \leftrightarrow \overline{A}$. Neglecting *CP* violation in charm decays, which is known to be small in D^0–$\overline{D}^0$ mixing and Cabibbo-favoured D meson decays [20], the conjugate amplitudes are related by $A(m^2_-, m^2_+) = \overline{A}(m^2_+, m^2_-)$.

The Dalitz plot is partitioned into $2N$ regions symmetric under the exchange $m^2_+ \leftrightarrow m^2_-$, following Ref. [7]. The bins are labelled from $-N$ to $+N$ (excluding zero), where the positive bins have $m^2_- > m^2_+$. At each point in the Dalitz plot, there is a strong-phase difference $\delta_D(m^2_-, m^2_+) \equiv \arg A - \arg \overline{A}$ between the D^0 and $\overline{D}^0$ decay. The cosine of the strong-phase difference averaged in each bin and weighted by the decay rate is termed c_i and is given by

$$c_i \equiv \frac{\int_{\mathcal{D}_i} (|A||\overline{A}| \cos\delta_D)\, d\mathcal{D}}{\sqrt{\int_{\mathcal{D}_i} |A|^2\, d\mathcal{D}} \sqrt{\int_{\mathcal{D}_i} |\overline{A}|^2\, d\mathcal{D}}}, \tag{2}$$

where the integrals are evaluated over the area $\mathcal{D}_i$ of bin i. An analogous expression may be written for s_i, which is the sine of the strong-phase difference within bin i, weighted by the decay rate. The values of c_i and s_i have been directly measured by the CLEO collaboration, exploiting quantum-correlated $D^0\overline{D}^0$ pairs produced at the $\psi(3770)$ resonance [18]. One D meson was reconstructed in a decay to either $K^0_S h^+ h^-$ or $K^0_L h^+ h^-$, and the other D meson was reconstructed either in a *CP* eigenstate or in a decay to $K^0_S h^+ h^-$. The efficiency-corrected event yields, combined with flavour-tag information, allowed c_i and s_i to be determined. There is a systematic uncertanty associated with using these direct measurements due their finite precision. The alternative is to calculate c_i and s_i assuming a functional form for $|A|$, $|\overline{A}|$ and δ_D, which may be obtained from an amplitude model fitted to flavour-tagged D^0 decays. This alternative method relies on assumptions about the nature of the intermediate resonances that contribute to the $K^0_S h^+ h^-$ final state, and leads to a systematic uncertainty associated with the variation in δ_D.

In the CLEO-c study the $K^0_S \pi^+ \pi^-$ Dalitz plot was partitioned into 2×8 bins, with a number of schemes available. The 'optimal binning' variant [18], where the bins have been chosen to optimise the statistical sensitivity to γ, is adopted in this analysis. The optimisation was performed assuming a strong-phase difference distribution as given by the BaBar model presented in Ref. [10]. For the $K^0_S K^+ K^-$ final state, c_i and s_i measurements are available for the Dalitz plot partitioned into different numbers of bins with the guiding model being that from the BaBar study described in Ref. [11]. The analysis described here adopts the 2×2 option, a decision driven by the size of the signal sample. The use of a specific model in defining the bin boundaries does not bias the c_i and s_i measurements. If the model is a poor description of the underlying decay the only consequence is a reduction in the statistical sensitivity of the γ measurement. The binning choices for the two decay modes are shown in Fig. 1.

The population of each positive (negative) bin in the Dalitz plot arising from B^+ decays is N^+_{+i} (N^+_{-i}), and that from B^- decays is N^-_{+i} (N^-_{-i}). The physics parameters of

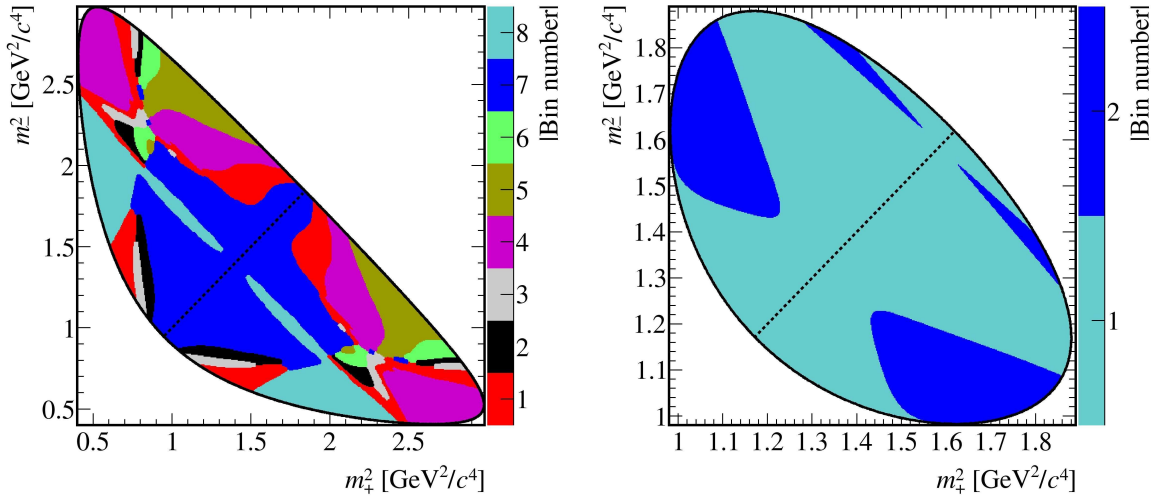

Figure 1: Binning schemes for (left) $D \to K^0_S\pi^+\pi^-$ and (right) $D \to K^0_S K^+ K^-$. The diagonal line separates the positive and negative bins, where the positive bins are in the region where $m^2_- > m^2_+$ is satisfied.

interest, r_B, δ_B, and γ, are translated into four *CP* observables [9] that are measured in this analysis. These observables are defined as

$$x_\pm \equiv r_B \cos(\delta_B \pm \gamma) \quad \text{and} \quad y_\pm \equiv r_B \sin(\delta_B \pm \gamma). \tag{3}$$

The selection requirements introduce nonuniformities in the populations of the Dalitz plot. The relative selection and reconstruction efficiency profile $\varepsilon = \varepsilon(m^2_-, m^2_+)$ for signal candidates is defined as a function of the position in the Dalitz plot. The absolute normalisation of ε is not relevant; only the efficiency associated with one point relative to the others matters. Considering Eq. 1 it follows that

$$\begin{aligned} N^+_{\pm i} &= h_{B^+}\left[F_{\mp i} + (x_+^2 + y_+^2)F_{\pm i} + 2\sqrt{F_i F_{-i}}(x_+ c_{\pm i} - y_+ s_{\pm i})\right], \\ N^-_{\pm i} &= h_{B^-}\left[F_{\pm i} + (x_-^2 + y_-^2)F_{\mp i} + 2\sqrt{F_i F_{-i}}(x_- c_{\pm i} + y_- s_{\pm i})\right], \end{aligned} \tag{4}$$

where the value F_i is given by

$$F_i = \frac{\int_{\mathcal{D}_i} |A|^2\, \varepsilon\, d\mathcal{D}}{\sum_j \int_{\mathcal{D}_j} |A|^2\, \varepsilon\, d\mathcal{D}} \tag{5}$$

and is the fraction of events in bin i of the $D^0 \to K^0_S h^+ h^-$ Dalitz plot. The quantities $h_{B^\pm}$ are normalisation factors, which can be different for B^+ and B^- due to asymmetries in production rates of bottom and antibottom mesons.

The observed distribution of candidates over the $D \to K^0_S h^+ h^-$ Dalitz plot is used to fit for $x_\pm$, $y_\pm$ and $h_{B^\pm}$. The values of F_i are determined from the control mode $\overset{(-)}{B} \to D^{*\pm}\mu^{\mp}\overset{(-)}{\nu}_{\mu} X$, where the $D^{*\pm}$ decays to $\overset{(-)}{D}{}^0\pi^\pm$, and the $\overset{(-)}{D}{}^0$ decays to either the $K^0_S\pi^+\pi^-$ or $K^0_S K^+ K^-$ final state. The symbol X, hereinafter omitted, indicates other particles that are potentially produced in the $\overset{(-)}{B}$ decay. Samples of simulated events are used to correct for differences in the efficiency for reconstructing and selecting $\overset{(-)}{B} \to D^{*\pm}\mu^{\mp}\overset{(-)}{\nu}_{\mu}$ and $B^\pm \to DK^\pm$ decays.

In addition to selecting $B^\pm \to DK^\pm$ and $\overset{(-)}{B} \to D^{*\pm}\mu^{\mp}\overset{(-)}{\nu}_{\mu}$ candidates we also select $B^\pm \to D\pi^\pm$ decays. Candidates selected in this decay mode provide an important control sample that is used to constrain the invariant mass shape of the $B^\pm \to DK^\pm$ signal and to determine the yield of $B^\pm \to D\pi^\pm$ decays misidentified as $B^\pm \to DK^\pm$ candidates.

The use of $\overset{(-)}{B} \to D^{*\pm}\mu^{\mp}\overset{(-)}{\nu}_{\mu}$ decays to determine the values of F_i is an improvement over Ref. [4], for which the decay $B^\pm \to D\pi^\pm$ was used. The small level of *CP* violation in the latter decay led to a significant systematic uncertainty. This uncertainty is eliminated when using the flavour-specific semileptonic decay. There is still a systematic uncertainty associated with the procedure but it is relatively small in magnitude.

The effect of D^0–$\overline{D}{}^0$ mixing is ignored in the above discussion, and was neglected in the CLEO-c measurements of c_i and s_i as well as in the values of F_i. This leads to a bias of approximately 0.2° in the γ determination [21], which is negligible for the current analysis. The effect of *CP* violation in K^0_S decays is expected to lead to a $\mathcal{O}(1^\circ)$ uncertainty [22], and is also ignored given the expected precision. An uncertainty due to the different nuclear interaction cross sections for K^0 and $\overline{K}{}^0$ mesons is expected to be of a similar magnitude and is also ignored [23].

The rest of the paper is organised as follows. Section 3 describes the LHCb detector, and Section 4 presents the selection and the model used to fit the invariant mass spectrum. Sections 5 and 6 are concerned with the selection of the semileptonic control channel, used to determine the signal efficiency profile. Section 7 discusses the binned Dalitz plot fit and presents the results for the *CP* parameters. The evaluation of systematic uncertainties is summarised in Section 8. In Section 9 the use of the measured *CP* parameters to determine the CKM angle γ is described. The results of the analysis are summarised in Section 10.

3 Detector and simulation

The LHCb detector [24] is a single-arm forward spectrometer covering the pseudorapidity range $2 < \eta < 5$, designed for the study of particles containing b or c quarks. The detector includes a high-precision tracking system consisting of a silicon-strip vertex detector surrounding the pp interaction region, a large-area silicon-strip detector located upstream of a dipole magnet with a bending power of about 4 Tm, and three stations of silicon-strip detectors and straw drift tubes [25] placed downstream. The combined tracking system provides a momentum measurement with relative uncertainty that varies from 0.4% at 2 GeV/c to 0.6% at 100 GeV/c, and impact parameter resolution of 20 μm for tracks with large transverse momentum. Different types of charged hadrons are distinguished

using information from two ring-imaging Cherenkov detectors [26]. Photon, electron and hadron candidates are identified by a calorimeter system consisting of scintillating-pad and preshower detectors, an electromagnetic calorimeter and a hadronic calorimeter. Muons are identified by a system composed of alternating layers of iron and multiwire proportional chambers [27]. The trigger [28] consists of a hardware stage, based on information from the calorimeter and muon systems, followed by a software stage, which applies a full event reconstruction. The trigger algorithms used to select candidate fully hadronic and semileptonic B decays are slightly different due to the presence of the muon in the latter.

In the simulation, pp collisions are generated using Pythia [29, 30] with a specific LHCb configuration [31]. Decays of hadronic particles are described by EvtGen [32], in which final-state radiation is generated using Photos [33]. The interaction of the generated particles with the detector and its response are implemented using the Geant4 toolkit [34, 35] as described in Ref. [36].

4 Event selection and fit to invariant mass spectrum for $B^\pm \to DK^\pm$ and $B^\pm \to D\pi^\pm$ decays

Selection requirements are applied to obtain an event sample enriched with $B^\pm \to DK^\pm$ and $B^\pm \to D\pi^\pm$ candidates, where D indicates a D^0 or $\overline{D}{}^0$ meson that decays to the final state $K^0_{\rm S}h^+h^-$. The kaon or pion produced directly in the $B^\pm$ decay is denoted the 'bachelor' hadron. Decays of $K^0_{\rm S}$ mesons to the $\pi^+\pi^-$ final state are reconstructed in two different categories, the first involving $K^0_{\rm S}$ mesons that decay early enough for the pions to be reconstructed in the vertex detector, the second containing $K^0_{\rm S}$ that decay later such that track segments of the pions cannot be formed in the vertex detector. These categories are referred to as *long* and *downstream*, respectively. The candidates in the long category have better mass, momentum and vertex resolution than those in the downstream category. Henceforth $B^\pm$ candidates are denoted long or downstream depending on which $K^0_{\rm S}$ type they contain.

Events considered in the analysis must fulfil both hardware and software trigger requirements. At the hardware stage at least one of the two following criteria must be satisfied: either a particle produced in the decay of the signal $B^\pm$ candidate leaves a deposit with high transverse energy in the hadronic calorimeter, or the event is accepted because particles not associated with the signal candidate fulfil the trigger requirements. The software trigger designed to select $B^\pm \to DK^\pm$ and $B^\pm \to D\pi^\pm$ candidates requires a two-, three- or four-track secondary vertex with a large sum of the transverse momentum, $p_{\rm T}$, of the associated charged particles and a significant displacement from the primary pp interaction vertices (PVs). At least one charged particle should have $p_{\rm T} > 1.7\,{\rm GeV}/c$ and $\chi^2_{\rm IP}$ with respect to any primary interaction greater than 16, where $\chi^2_{\rm IP}$ is defined as the difference in χ^2 of a given PV fitted with and without the considered track. A multivariate algorithm [37] is used for the identification of secondary vertices that are consistent with the decay of a b hadron.

A multivariate approach is employed to improve the event selection relative to that

used in Ref. [4]. A boosted decision tree [38, 39] (BDT) is trained on simulated signal events and background taken from the high $B^\pm$ mass sideband (5800–7000 MeV/c^2). Both signal and background samples contain candidates from the D and K^0_S signal regions only. Different BDTs are trained for long and downstream candidates. Each BDT uses the following variables: the logarithm of the $\chi^2_{\rm IP}$ of the pions from the D decay and also of the bachelor particle; the logarithm of the $\chi^2_{\rm IP}$ of the K^0_S decay products (long candidates only); the logarithm of the D $\chi^2_{\rm IP}$; the $B^\pm$ $\chi^2_{\rm IP}$; a variable characterising the $B^\pm$ flight distance; the $B^\pm$ and D momenta; the χ^2 of the kinematic fit of the whole decay chain, (described in detail below); and the '$B^\pm$ isolation variable', a quantity designed to ensure the $B^\pm$ candidate is well isolated from other tracks in the event. The $B^\pm$ isolation variable is the asymmetry between the $p_{\rm T}$ of the signal candidate and the vector sum of the $p_{\rm T}$ of the other tracks in the event that lie within a distance of 1.5 rad in η–ϕ space, where ϕ is the azimuthal angle. The discriminating power of the variables differs slightly for long and downstream candidates. Two variables that are highly discriminating for both samples are the $B^\pm$ $\chi^2_{\rm IP}$ and $B^\pm$ isolation variable. An optimal value of the BDT discriminator is determined with a series of pseudo-experiments to obtain the value that provides the best sensitivity to $x_\pm$, $y_\pm$. Events in the data sample that have a value below the optimum are rejected. The optimal BDT value is different for long and downstream candidates primarily because the level of combinatorial background is larger for the latter.

To suppress background further, the K^0_S, D and $B^\pm$ momentum vectors are required to point in the same direction as the vector connecting their production and decay vertices. The mass of the D candidate must lie within 25 MeV/c^2 of the known D mass [20].

Particle identification (PID) requirements are placed on the bachelor to separate $B^\pm \to DK^\pm$ and $B^\pm \to D\pi^\pm$ candidates. PID criteria are also applied to the kaons from the D decay for the final state $K^0_S K^+ K^-$. To ensure good control of the PID performance it is required that information from the RICH detectors is present.

A kinematic fit [40] is imposed on the full $B^\pm$ decay chain. The fit constrains the $B^\pm$ candidate to point towards the PV and the D and K^0_S candidates to have their known masses [20]. This fit improves the $B^\pm$ mass resolution and therefore provides greater discrimination between signal and background; furthermore, it improves the resolution on the Dalitz plot and ensures that all candidates lie within the kinematically-allowed region of the Dalitz plot. The candidates obtained in this fit are used to determine the physics parameters of interest. An additional fit, in which only the $B^\pm$ pointing and D mass constraints are imposed, is employed to aid discrimination between genuine and background K^0_S candidates. After this fit is applied it is required that the mass of the K^0_S candidate lies within 15 MeV/c^2 of its known value [20].

To remove background from $D \to \pi^+\pi^-\pi^+\pi^-$ decays, long K^0_S candidates are required to have travelled a significant distance from the D vertex. To remove charmless $B^\pm$ decays, the displacement along the beamline between the D and $B^\pm$ decay vertices is required to be positive.

The invariant mass distributions of the selected candidates are shown in Fig. 2 for $B^\pm \to DK^\pm$ and $B^\pm \to D\pi^\pm$, with $D \to K^0_S\pi^+\pi^-$ decays, divided between the long and downstream K^0_S categories. Figure 3 shows the corresponding distributions for final

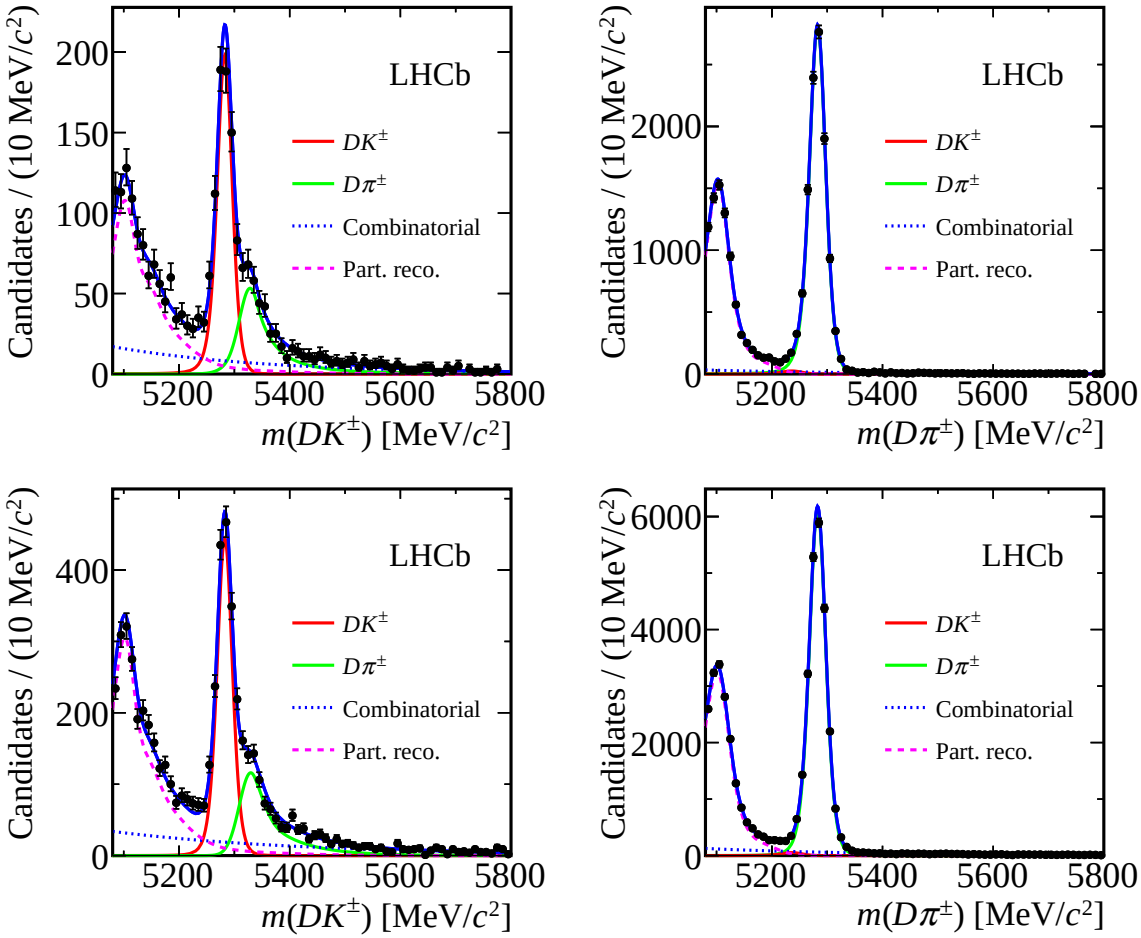

Figure 2: Invariant mass distributions of (left) $B^\pm \to DK^\pm$ and (right) $B^\pm \to D\pi^\pm$ candidates, with $D \to K^0_S\pi^+\pi^-$, divided between the (top) long and (bottom) downstream K^0_S categories. Fit results, including the signal and background components, are superimposed.

states with $D \to K^0_S K^+ K^-$. The result of an extended maximum likelihood fit to these distributions is superimposed. The fit is performed simultaneously for $B^\pm \to DK^\pm$ and $B^\pm \to D\pi^\pm$ candidates, including both $D \to K^0_S\pi^+\pi^-$ and $D \to K^0_S K^+ K^-$ decays, allowing several independent parameters for long and downstream K^0_S categories. The fit range is between 5080 MeV/c^2 and 5800 MeV/c^2 in the $B^\pm$ invariant mass. The purpose of this simultaneous fit to data integrated over the Dalitz plot is to determine the parameters that describe the invariant mass spectrum in preparation for the binned fit described in Sect. 7. The mass spectrum of $B^\pm \to D\pi^\pm$ candidates is fitted because it is similar to the $B^\pm \to DK^\pm$ spectrum, aiding the determination of the signal lineshape due to the higher yield and lower background. The yield of $B^\pm \to D\pi^\pm$ candidates misidentified as $B^\pm \to DK^\pm$ candidates can be determined from knowledge of the $B^\pm \to D\pi^\pm$ signal yield and the PID selection efficiencies.

The signal probability density function (PDF) is a Gaussian function with asymmetric

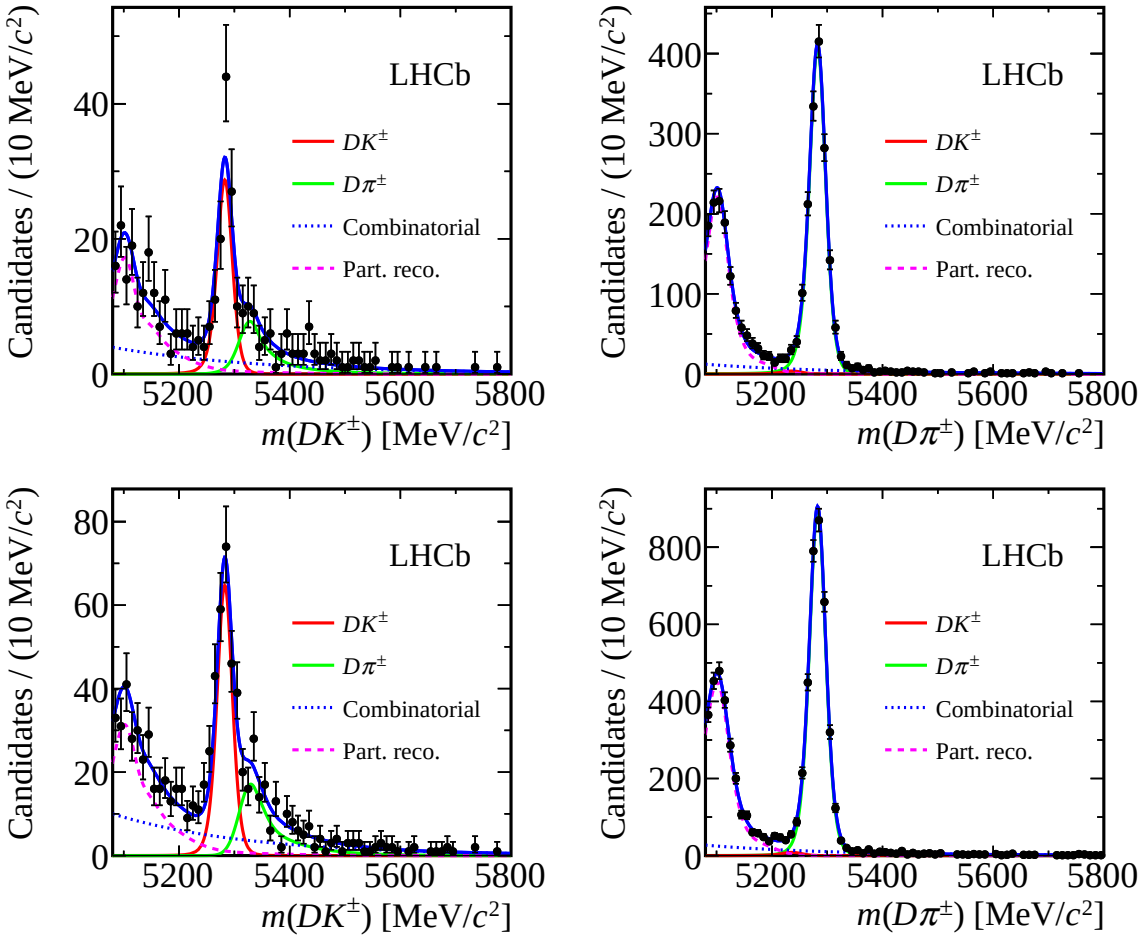

Figure 3: Invariant mass distributions of (left) $B^\pm \to DK^\pm$ and (right) $B^\pm \to D\pi^\pm$ candidates, with $D \to K^0_S K^+ K^-$, divided between the (top) long and (bottom) downstream K^0_S categories. Fit results, including the signal and background components, are superimposed.

tails, defined as

$$f(m; m_0, \sigma, \alpha_L, \alpha_R) \propto \begin{cases} \exp[-(m-m_0)^2/(2\sigma^2 + \alpha_L(m-m_0)^2)] & m < m_0 \\ \exp[-(m-m_0)^2/(2\sigma^2 + \alpha_R(m-m_0)^2)] & m > m_0 \end{cases} \quad (6)$$

where m is the candidate mass and m_0, σ, α_L, and α_R are free parameters in the fit. The parameter m_0 is common to all classes of signal. The parameters describing the asymmetric tails, $\alpha_{L,R}$, are fitted separately for events with long and downstream K^0_S categories. The width parameter σ is left as a free parameter for the two K^0_S categories, but the ratio between this width in $B^\pm \to DK^\pm$ and $B^\pm \to D\pi^\pm$ decays is required to be the same, independent of K^0_S reconstruction or D^0 decay category. The width is determined to be around 13 MeV/c^2 for $B^\pm \to DK^\pm$ decays of both K^0_S classes, and is 10% larger for $B^\pm \to D\pi^\pm$ decays. The yield of $B^\pm \to D\pi^\pm$ candidates in each category is determined

in the fit. Instead of fitting the yield of the $B^\pm \to DK^\pm$ candidates separately, the ratio $\mathcal{R} \equiv N(B^\pm \to DK^\pm)/N(B^\pm \to D\pi^\pm)$ is determined and is constrained to have the same value for all categories.

The background has contributions from random track combinations and partially reconstructed B decays. The random track combinations are modelled by exponential PDFs. The slopes of these functions are determined through the study of two independent samples: candidates reconstructed such that both charged hadrons produced in the D decay have the same sign, and candidates reconstructed using the D mass sidebands. The slopes are consistent with each other. In the fit to the signal data the exponential slopes are Gaussian-constrained to the results of the sideband studies.

A significant background component exists in the $B^\pm \to DK^\pm$ sample, arising from a fraction of the dominant $B^\pm \to D\pi^\pm$ decays in which the bachelor particle is misidentified as a kaon by the RICH system. The yield of this type of background is calculated using knowledge of misidentification efficiencies that are obtained from large samples of kinematically selected $D^{*\pm} \to {}^{(}\overline{D}{}^{)0}\pi^\pm$, ${}^{(}\overline{D}{}^{)0} \to K^\mp\pi^\pm$ decays. The tracks in this calibration sample are reweighted to match the momentum and pseudorapidity distributions of the bachelor tracks in the $B^\pm$ decay sample, thereby ensuring that the measured PID performance is representative of that in the $B^\pm$ decay sample. The efficiency to identify a kaon correctly is found to be 86%, and that for a pion to be 96%. The efficiency of misidentifying a pion as a kaon is 4%. From this information and from the knowledge of the number of reconstructed $B^\pm \to D\pi^\pm$ decays, the amount of this background surviving the $B^\pm \to DK^\pm$ selection is estimated.

The distribution of true $B^\pm \to D\pi^\pm$ candidates misidentified as $B^\pm \to DK^\pm$ candidates is determined using data. The $B^\pm$ invariant mass distribution is obtained by reconstructing candidates in the $B^\pm \to D\pi^\pm$ sample with a kaon mass hypothesis for the bachelor pion. The sample is weighted using the *sPlot* method [41] and the PID efficiencies. The use of the *sPlot* method in the reweighting suppresses partially reconstructed and combinatorial backgrounds. Weighting by PID efficiencies allows for reproduction of the kinematic properties of pions misidentified as kaons in the signal $B^\pm \to DK^\pm$ sample. The weighted distribution is fitted to a parametric shape with different shapes used for the samples containing long and downstream $K^0_{\rm S}$ decays. The fitted parameters are subsequently fixed in the fit to the $B^\pm$ invariant mass spectrum.

A similar procedure is used to determine the number of $B^\pm \to DK^\pm$ decays misidentified as $B^\pm \to D\pi^\pm$. Due to the reduced branching fraction of $B^\pm \to DK^\pm$ and the small likelihood of misidentifying a kaon as a pion, such cases occur at a low rate and have a minor influence on the fit.

Partially reconstructed b-hadron decays (shown as Part. Reco. in Fig. 2 and Fig. 3) contaminate the sample predominantly at invariant masses smaller than that of the signal peak. These decays contain an unreconstructed pion or a photon, which comes from a vector-meson decay. The dominant decays in the signal region are $B^\pm \to D\rho^\pm$, $B^\pm \to D^{*0}\pi^\pm$ and $B^0 \to D^{*\pm}\pi^\mp$ decays in which one particle is missed. The distribution in the invariant mass spectrum depends on the spin and mass of the missing particle. If the missing particle has spin-parity $J^P = 0^-$ (1^-), the distribution is parameterised

Table 1: Yields and statistical uncertainties in the signal region from the invariant mass fits, scaled from the full fit mass range, for candidates passing the $B^\pm \to D(K^0_S\pi^+\pi^-)h^\pm$ selection. Values are shown separately for candidates formed using long and downstream K^0_S decays. The signal region is between 5247 MeV/c^2 and 5317 MeV/c^2 and the full fit range is between 5080 MeV/c^2 and 5800 MeV/c^2.

Fit component	$B^\pm \to DK^\pm$ selection		$B^\pm \to D\pi^\pm$ selection	
	Long	Downstream	Long	Downstream
$B^\pm \to DK^\pm$	702 ± 18	1555 ± 39	30 ± 5	64 ± 7
$B^\pm \to D\pi^\pm$	87 ± 9	164 ± 13	10 338 ± 106	22 779 ± 166
Combinatorial	59 ± 9	133 ± 14	103 ± 11	433 ± 25
Partially reconstructed	38 ± 2	82 ± 3	4.6 ± 0.1	14.2 ± 0.1

Table 2: Yields and statistical uncertainties in the signal region from the invariant mass fits, scaled from the full fit mass range, for candidates passing the $B^\pm \to D(K^0_S K^+K^-)h^\pm$ selection. Values are shown separately for candidates formed using long and downstream K^0_S decays. The signal region is between 5247 MeV/c^2 and 5317 MeV/c^2 and the full fit range is between 5080 MeV/c^2 and 5800 MeV/c^2.

Fit component	$B^\pm \to DK^\pm$ selection		$B^\pm \to D\pi^\pm$ selection	
	Long	Downstream	Long	Downstream
$B^\pm \to DK^\pm$	101 ± 4	223 ± 7	4.5 ± 1.9	10.1 ± 2.9
$B^\pm \to D\pi^\pm$	13 ± 3	24 ± 5	1501 ± 38	3338 ± 57
Combinatorial	13 ± 3	30 ± 5	36 ± 5	78 ± 7
Partially reconstructed	4.6 ± 0.7	8.6 ± 1.2	0.60 ± 0.02	2.0 ± 0.1

with a parabola with positive (negative) curvature convolved with a resolution function. The mass of the missing particle defines the kinematic endpoints of the distribution prior to reconstruction. The shapes for decays in which a particle is missed and a pion is misidentified as a kaon are parameterised with semi-empirical PDFs formed from sums of Gaussian and error functions. The parameters of these distributions are fixed to the results of fits to data from two-body D decays, with the exception of the resolution function width, the ratio of widths in the $B^\pm \to DK^\pm$ and $B^\pm \to D\pi^\pm$ channels and a shift along the $B^\pm$ mass. The resulting PDF is cross-checked with a similar fit to an admixture of simulated backgrounds.

The number of $B^\pm \to DK^\pm$ candidates in each K^0_S category or D^0 decay category is determined from the value of $\mathcal{R}$ and the number of $B^\pm \to D\pi^\pm$ events in the corresponding category. The ratio $\mathcal{R}$ is determined in the fit and measured to be $(7.7 \pm 0.2)\%$ (statistical uncertainty only), consistent with that observed in Ref. [1]. The yields returned by the invariant mass fit in the full fit region are scaled to the signal region, defined as 5247–5317 MeV/c^2, and are presented in Tables 1 and 2. Because the $B^\pm \to DK^\pm$ yields are calculated using $\mathcal{R}$ their uncertainties are smaller than those that would be expected if the yields were allowed to vary in the fit.

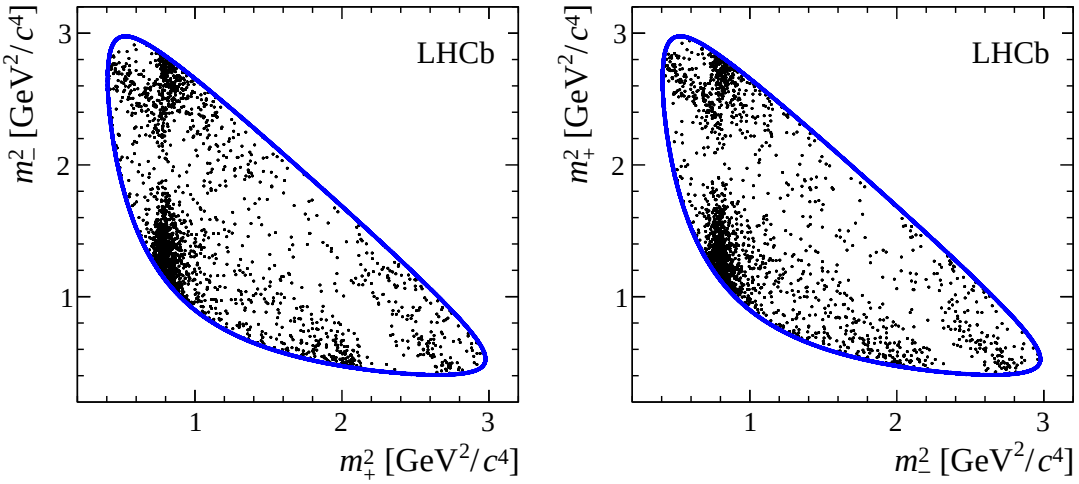

Figure 4: Dalitz plots of $B^\pm \to DK^\pm$ candidates in the signal region for $D \to K^0_S\pi^+\pi^-$ decays from (left) B^+ and (right) B^- decays. Both long and downstream K^0_S candidates are included. The blue line indicates the kinematic boundary.

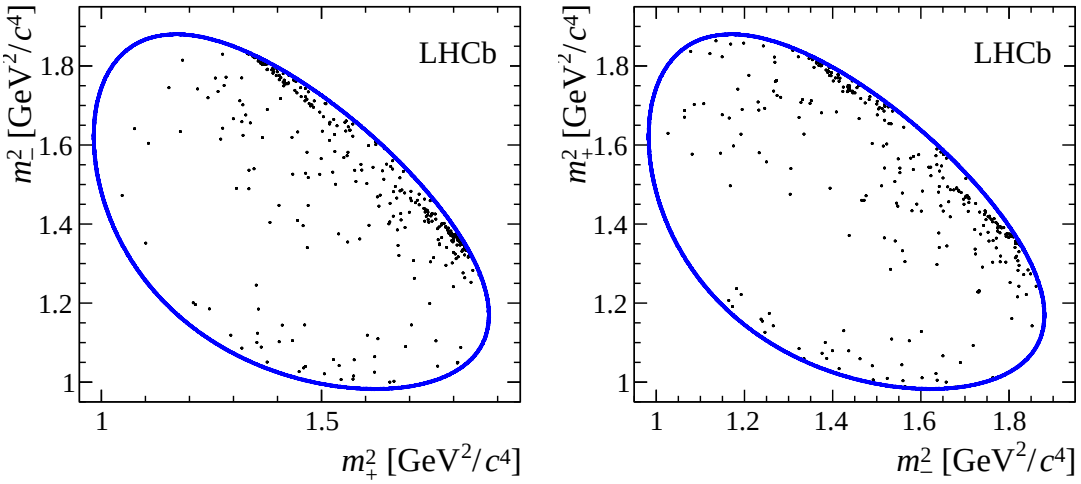

Figure 5: Dalitz plots of $B^\pm \to DK^\pm$ candidates in the signal region for $D \to K^0_S K^+K^-$ decays from (left) B^+ and (right) B^- decays. Both long and downstream K^0_S candidates are included. The blue line indicates the kinematic boundary.

The Dalitz plots for $B^\pm \to DK^\pm$ candidates restricted to the signal region for the two $D \to K^0_S h^+h^-$ final states are shown in Figs. 4 and 5. Separate plots are shown for B^+ and B^- decays.

5 Event selection and yield determination for $\overline{(}B\overline{)} \to D^{*\pm}\mu^{\mp}\overline{(}\nu_\mu\overline{)}$ decays

A sample of the decays $\overline{(}B\overline{)} \to D^{*\pm}\mu^{\mp}\overline{(}\nu_\mu\overline{)}$, $D^{*\pm} \to \overline{(}D\overline{)}^0\pi^\pm$, $\overline{(}D\overline{)}^0 \to K^0_{\rm S}h^+h^-$ is used to determine the quantities F_i. These are defined in Eq. 5 as the expected fractions of D^0 decays falling into the Dalitz plot bin labelled i, taking into account the efficiency profile of the signal decay. The semileptonic decay of the B and the strong-interaction decay of the $D^{*\pm}$ allow the flavour of the D^0 meson to be determined from the charge of the bachelor muon and pion. This particular decay chain, involving a flavour-tagged D^0 decay, is chosen due to its low background level and low mistag probability. The selection requirements are chosen to minimise changes to the efficiency profile with respect to that associated with the $B^\pm \to DK^\pm$ and $B^\pm \to D\pi^\pm$ sample. They are identical to the requirements listed in Sect. 4 where possible; the requirements on variables used to train the BDT follow those described in Ref. [4].

Candidate $\overline{(}B\overline{)} \to D^{*\pm}\mu^{\mp}\overline{(}\nu_\mu\overline{)}$ events are selected using information from the muon detector systems. These events are first required to pass the hardware trigger which selects muons with a transverse momentum $p_{\rm T} > 1.48\,{\rm GeV}/c$. Approximately 95% of the final $\overline{(}B\overline{)} \to D^{*\pm}\mu^{\mp}\overline{(}\nu_\mu\overline{)}$ sample is collected with this algorithm, and the remainder pass a hardware trigger which selects D^0 candidates that leave a high transverse energy deposit in the hadronic calorimeter. In the software trigger, at least one of the final-state particles is required to have both $p_{\rm T} > 0.8\,{\rm GeV}/c$ and impact parameter greater than 100 μm with respect to all of the PVs in the event. Finally, the tracks of two or more of the final-state particles are required to form a vertex that is significantly displaced from the PVs.

To reduce combinatorial background, all charged decay products are required to be inconsistent with originating from the PV, and the momentum vectors of the $K^0_{\rm S}$, D^0 and B are required to be aligned with the vector between their production and decay vertices. The B candidate vertex is required to be well separated from the PV in order to discriminate between B decays and prompt charm decays.

The B decay chain is refitted [40] to determine the distribution of candidates across the Dalitz plot. Unlike the refit performed for $B^\pm \to Dh^\pm$ candidates, the fit constrains only the D^0 and $K^0_{\rm S}$ candidates to their known masses as the B candidate is not fully reconstructed in the semileptonic decay mode. An additional fit, in which only the $K^0_{\rm S}$ mass is constrained, is performed to improve the D^0 and $D^{*\pm}$ mass resolutions for use in the invariant mass fit used to determine signal yields.

Additional requirements are included to remove $D^0 \to \pi^+\pi^-\pi^+\pi^-$ decays and charmless B decays, and PID criteria are placed on the kaons in $D^0 \to K^0_{\rm S}K^+K^-$. The requirements are the same as those applied to the $B^\pm \to DK^\pm$ and $B^\pm \to D\pi^\pm$ candidates described in Sect. 4. The $K^0_{\rm S}$ candidate mass is required to be within $20\,{\rm MeV}/c^2$ of the known value [20], and the invariant mass sum of the $D^{*\pm}$ and muon, determined using the refit containing the D^0 and $K^0_{\rm S}$ mass constraints, is required to be less than $5000\,{\rm MeV}/c^2$.

The candidate D^0 invariant mass, $m(K^0_{\rm S}h^+h^-)$, and the invariant mass difference $\Delta m \equiv m(K^0_{\rm S}h^+h^-\pi^\pm) - m(K^0_{\rm S}h^+h^-)$ are fitted simultaneously to determine the signal

yields. No significant correlation between these two variables is observed. This two-dimensional parameterisation allows the yield of selected candidates to be measured in three categories: true $D^{*\pm}$ candidates (signal), candidates containing a true D^0 but random soft pion (RSP) and candidates formed from random track combinations that fall within the fit range (combinatorial background). An example projection is shown in Fig. 6. The result of a two-dimensional extended, unbinned, maximum likelihood fit is superimposed. The fit is performed simultaneously for the two D^0 final states and the two $K^0_{\rm S}$ categories with some parameters allowed to be independent between categories. Candidates selected from data recorded in 2011 and 2012 are fitted separately, due to their slightly different Dalitz plot efficiency profiles. The fit range is $1830 < m(K^0_{\rm S}h^+h^-) < 1910\,{\rm MeV}/c^2$ and $139.5 < \Delta m < 153.0\,{\rm MeV}/c^2$. The $m(K^0_{\rm S}h^+h^-)$ range is chosen to be within a region where the Δm resolution does not vary significantly.

The signal is parameterised in Δm with a sum of two modified Gaussian PDFs, each given by

$$f(\Delta m;\mu_m,\sigma,\beta,\delta) = \frac{\delta\exp\left(-0.5\left[\beta+\delta\log\left(\frac{\Delta m-\mu_m}{\sigma}+\sqrt{1+\left(\frac{\Delta m-\mu_m}{\sigma}\right)^2}\right)\right]^2\right)}{\sigma\sqrt{2\pi[1+\left(\frac{\Delta m-\mu_m}{\sigma}\right)^2]}}, \quad (7)$$

where μ_m, σ, β and δ are floating parameters in the fit. The parameter μ_m is shared in all data categories and the remaining parameters are fitted separately for long and downstream $K^0_{\rm S}$ candidates. The combinatorial and RSP backgrounds are both parameterised with an empirical model given by

$$f(\Delta m;\Delta m_0,x,p_1,p_2) = \left[1-\exp\left(-\frac{\Delta m-\Delta m_0}{x}\right)\right]\left(\frac{\Delta m}{\Delta m_0}\right)^{p_1}+p_2\left(\frac{\Delta m}{\Delta m_0}-1\right) \quad (8)$$

for $\Delta m - \Delta m_0 > 0$ and $f(\Delta m) = 0$ otherwise, where Δm_0, x, p_1 and p_2 are floating parameters. The parameter Δm_0, which describes the kinematic threshold for a $D^{*\pm}\to\overline{(D)}{}^0\pi^\pm$ decay, is shared in all data categories, and for both the combinatorial and RSP shapes. The remaining parameters are determined separately for $K^0_{\rm S}\pi^+\pi^-$ and $K^0_{\rm S}K^+K^-$ candidates.

The signal and RSP PDFs in $m(K^0_{\rm S}h^+h^-)$ are described by Eq. 6, where m_0, σ, α_L, and α_R are all free parameters. All of the parameters in the signal and RSP PDFs are constrained to be the same since both describe a true D^0 candidate, but the parameters are fitted separately for $K^0_{\rm S}\pi^+\pi^-$ and $K^0_{\rm S}K^+K^-$, due to the different phase space available in the D^0 decay. The combinatorial background is parameterised by a second-order polynomial.

In total a sample with a signal yield of 123 600 candidates is selected. The size of the sample is approximately 40 times larger than the $B^\pm\to DK^\pm$ yield. The signal mass range is defined as 1840–1890 (1850–1880) ${\rm MeV}/c^2$ in $m(K^0_{\rm S}\pi^+\pi^-)$ ($m(K^0_{\rm S}K^+K^-)$) and 143.9–146.9 ${\rm MeV}/c^2$ in Δm. Within this range the background components account for 3–6% of the yield depending on the category.

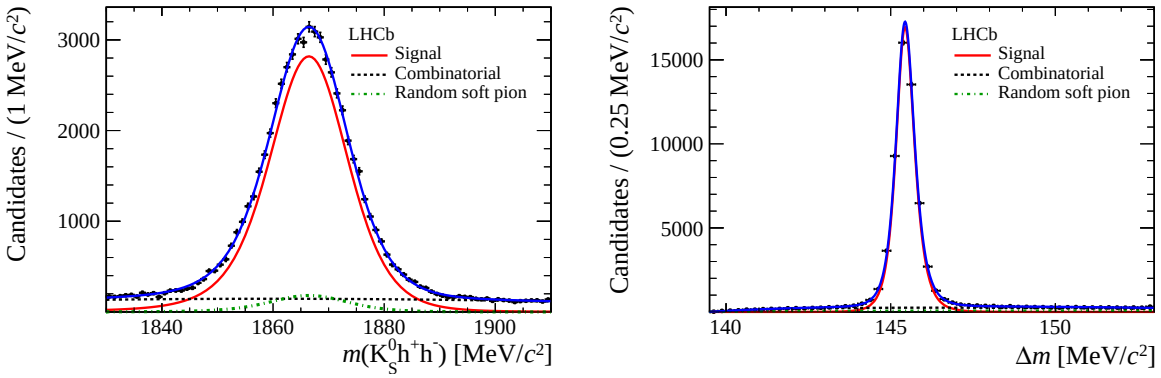

Figure 6: Result of the simultaneous fit to $\overline{(}B\overline{)} \to D^{*\pm}\mu^{\mp}\overline{(}\nu_\mu\overline{)}$, $D^{*\pm} \to \overline{(}D\overline{)}^0(\to K^0_S\pi^+\pi^-)\pi^\pm$ decays with downstream K^0_S candidates, in 2012 data. A two-dimensional fit is performed in (left) $m(K^0_S h^+ h^-)$ and (right) Δm. The (blue) total fit PDF is constructed from (solid red) signal, (dashed black) combinatorial background and (dotted green) random soft pion background.

6 Determining the F_i fractions from the semileptonic control channel

The two-dimensional fit in $m(K^0_S h^+ h^-)$ and Δm of the $\overline{(}B\overline{)} \to D^{*\pm}\mu^{\mp}\overline{(}\nu_\mu\overline{)}$ decay is repeated in each Dalitz plot bin, resulting in a raw control decay yield, R_i, for each bin i. Due to the differences in the efficiency profile over the Dalitz plot between D mesons originating from the control decay $\overline{(}B\overline{)} \to D^{*\pm}\mu^{\mp}\overline{(}\nu_\mu\overline{)}$ and those originating from the signal decay $B^\pm \to DK^\pm$, the measured relative proportions of the R_i values are not equivalent to the F_i fractions required to determine the CP parameters. The differences in the efficiency profiles, which originate from the different selections of the candidates from the signal and control decay modes, must be corrected for. The efficiency profiles from simulation of $D \to K^0_S\pi^+\pi^-$ decays are shown in Fig. 7. They show a variation of approximately 50% between the highest and lowest efficiency regions. The variation over the $D \to K^0_S K^+ K^-$ Dalitz plot is 35%. As the individual Dalitz plot bins cover regions of different efficiency the variation from the Dalitz plot bin with the highest efficiency and that with the lowest is approximately 30% (15%) for $D \to K^0_S\pi^+\pi^-$ ($D \to K^0_S K^+ K^-$) decays.

To understand the differences between the efficiency profiles of $\overline{(}B\overline{)} \to D^{*\pm}\mu^{\mp}\overline{(}\nu_\mu\overline{)}$ and $B^\pm \to DK^\pm$ decays, we compare the distributions of $\overline{(}B\overline{)} \to D^{*\pm}\mu^{\mp}\overline{(}\nu_\mu\overline{)}$ and $B^\pm \to D\pi^\pm$ observed in data and simulation. The reason for choosing $B^\pm \to D\pi^\pm$ is that the efficiency profile is the same as for $B^\pm \to DK^\pm$ (as verified in simulation), but the channel has higher yields than $B^\pm \to DK^\pm$. Moreover the $B^\pm \to D\pi^\pm$ has a level of interference, and hence CP violation, that is expected to be an order of magnitude smaller than in $B^\pm \to DK^\pm$, allowing the differences in efficiency profiles to be separated from differences arising from interference effects. The yield of $B^\pm \to D\pi^\pm$ candidates in each bin is determined by fitting the invariant mass spectrum of candidates in each bin using the parameterisation

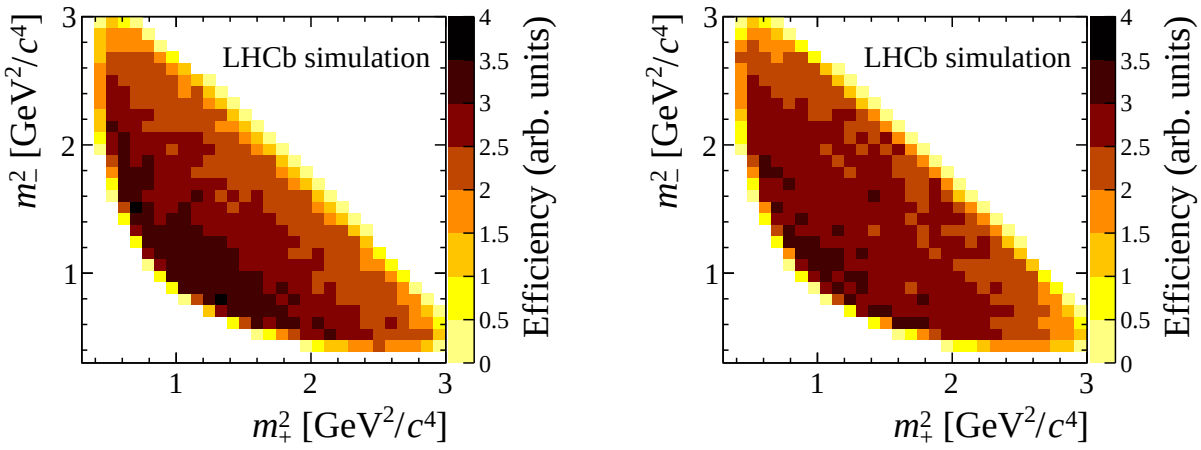

Figure 7: Example efficiency profiles of (left) $B^\pm \to D\pi^\pm$ and (right) $\overline{(}B\overline{)} \to D^{*\pm}\mu^\mp\overline{(}\nu_\mu\overline{)}$ decays in simulation. These plots refer to downstream K^0_S candidates under 2012 data taking conditions.

determined in Sect. 4.

Figure 8 shows the ratio of fractional signal yields, f_i, between $B^\pm \to D\pi^\pm$ and $\overline{(}B\overline{)} \to D^{*\pm}\mu^\mp\overline{(}\nu_\mu\overline{)}$ in each Dalitz plot bin. The ratios are averaged over the two K^0_S samples and two periods of data taking in different experimental conditions. To increase the sample size in each bin, the yield in bin i for $\overline{D}^0$ events is combined with the yield in bin $-i$ for D^0 events. Where the combination of yields is taken in this manner, exploiting the symmetry of the Dalitz plot, the bin number is referred to as the *effective* bin. Differences of up to 10% from unity are observed in the values of f_i. These cannot be explained by the small amount of *CP* violation in $B^\pm \to D\pi^\pm$ decays which is expected to vary the fractional yields by 3% or less, on the assumption that the magnitude of the interference in $B^\pm \to D\pi^\pm$ decays is $r^\pi_B = 0.01$.

The raw yields of the control decay must therefore be corrected to take into account the differences in efficiency profiles. For each Dalitz plot bin a correction factor is determined,

$$\xi_i \equiv \frac{\int_{\mathcal{D}_i} \varepsilon_{DK}\,|A|^2\,d\mathcal{D}}{\int_{\mathcal{D}_i} \varepsilon_{D^*\mu}\,|A|^2\,d\mathcal{D}}, \tag{9}$$

where ε_{DK} and $\varepsilon_{D^*\mu}$ are the efficiency profiles of the $B^\pm \to DK^\pm$ and $\overline{(}B\overline{)} \to D^{*\pm}\mu^\mp\overline{(}\nu_\mu\overline{)}$ decays, respectively, and $|A|^2$ is the Dalitz plot intensity for the D^0 decay. The amplitude models used to determine the Dalitz plot intensity for the correction factor are those from Ref. [10] and Ref. [11] for the $K^0_S\pi^+\pi^-$ and $K^0_S K^+K^-$ decays, respectively. The amplitude models used here only provide a description of the intensity distribution over the Dalitz plot and introduce no significant model dependence into the analysis. The simulation is used to determine the efficiency profiles ε_{DK} and $\varepsilon_{D^*\mu}$. The simulations are generated assuming a flat distribution across the $K^0_S h^+h^-$ phase space; hence the distribution of simulated events after triggering, reconstruction and selection is directly

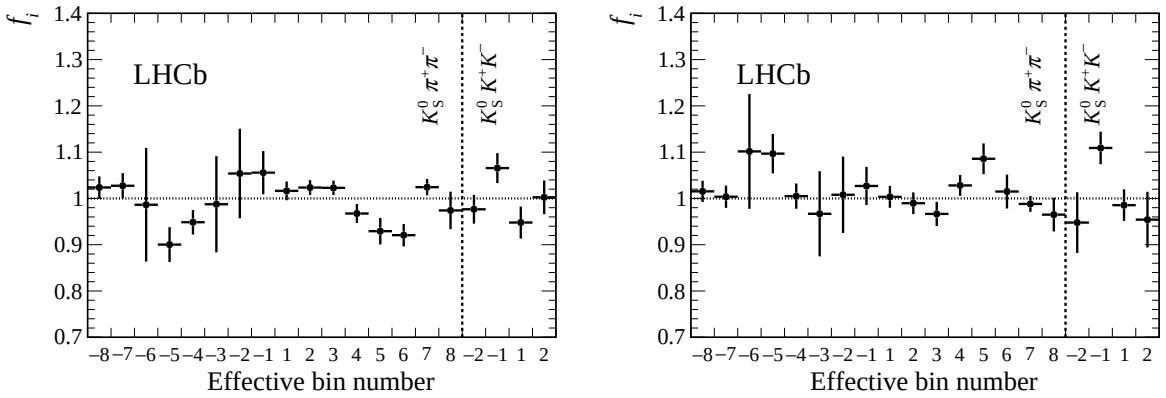

Figure 8: Fractional yield ratios of $B^\pm \to D\pi^\pm$ to $\overline{(B)} \to D^{*\pm}\mu^{\mp}\overline{(\nu)}_\mu$ decays, f_i, for each effective Dalitz plot bin. The vertical dashed line separates the ratios for $K^0_S\pi^+\pi^-$ (bins -8 to 8) and $K^0_S K^+K^-$ (bins -2 to 2). The left (right) plot shows the values of f_i before (after) correcting for the efficiency differences.

proportional to the efficiency profile. The correction factors are determined separately for data reconstructed with each K^0_S type as the efficiency profile is different between the two K^0_S categories.

The F_i values can be determined via the relation $F_i = h'\xi_i R_i$, where h' is a normalisation factor such that the sum of all F_i is unity. The total uncertainty on F_i is a combination of the uncertainty on R_i due to the size of the control channel, and the uncertainty on ξ_i due to the limited size of the simulated samples. The two contributions are similar in size.

To check the effect of the correction, the resulting F_i values are compared to the observed population as a function of the Dalitz plot in $B^\pm \to D\pi^\pm$ data. Figure 8, showing the ratio of $B^\pm \to D\pi^\pm$ fractional yields to raw $\overline{(B)} \to D^{*\pm}\mu^{\mp}\overline{(\nu)}_\mu$ fractional yields, gives a χ^2 per degree of freedom (χ^2/ndf) of 48.1/20 when considering the deviation from unity. When the corrected $\overline{(B)} \to D^{*\pm}\mu^{\mp}\overline{(\nu)}_\mu$ yields are used the fit quality improves to $\chi^2/\text{ndf} = 29.5/20$ as seen in Fig. 8. Although the χ^2 is calculated with respect to unity, the true value of F_i in each bin has a variation of order 3% due to *CP* violation in the $B^\pm \to D\pi^\pm$ decay.

7 Dalitz plot fit

The Dalitz plot fit is used to measure the *CP*-violating parameters $x_\pm$ and $y_\pm$, as introduced in Sect. 2. Following Eq. 4, these parameters can be determined from the populations of each $B^\pm \to DK^\pm$ Dalitz plot bin, given the external information from the c_i, s_i parameters from CLEO-c and the values of F_i from the semileptonic control decay modes.

Although the absolute numbers of B^+ and B^- decays integrated over the Dalitz plot have some dependence on $x_\pm$ and $y_\pm$, the sensitivity gained compared to using just the relative bin-to-bin yields is negligible. Consequently the integrated yields are not used and

the analysis is insensitive to charged B meson production and detection asymmetries. The observed size of the asymmetry of the integrated yields is consistent with that expected from the production and detection asymmetries, and the dependence on $x_\pm$ and $y_\pm$.

A simultaneous fit is performed on the $B^\pm \to Dh^\pm$ data, which are further split into the two B charges, the two K^0_S categories, the $B^\pm \to DK^\pm$ and $B^\pm \to D\pi^\pm$ candidates, and the two $D \to K^0_S h^+ h^-$ final states. The $B^\pm \to DK^\pm$ and $B^\pm \to D\pi^\pm$ samples are fitted simultaneously because the yield of $B^\pm \to D\pi^\pm$ signal in each Dalitz plot bin is used to determine the yield of misidentified events in the corresponding $B^\pm \to DK^\pm$ Dalitz plot bin. The PDF parameters for both the signal and background invariant mass distributions are fixed to the values determined in the invariant mass fit described in Sect. 4. The B mass range is reduced to 5150–5800 GeV/c^2 to reduce systematic uncertainties from the partially reconstructed background. The yields of all background contributions in each bin are free parameters, apart from the yields in bins in which an auxiliary fit determines the yield to be negligible. These are set to zero to facilitate the calculation of the uncertainty matrix. The yields of signal candidates for each bin in the $B^\pm \to D\pi^\pm$ sample are also free parameters. The amount of signal in each bin for the $B^\pm \to DK^\pm$ sample is determined by varying the integrated yield over all Dalitz plot bins and the $x_\pm$ and $y_\pm$ parameters. In the fit the values of F_i are Gaussian-constrained within their uncertainties. The values of c_i and s_i are fixed to their central values. In order to assess the impact of the $D \to K^0_S K^+ K^-$ data, the fit is then repeated including only the $D \to K^0_S \pi^+ \pi^-$ sample.

A large ensemble of pseudo-experiments is performed to validate the fit procedure. In each pseudo-experiment the numbers and distribution of signal and background candidates are generated according to the expected distribution in data, and the full fit procedure is then executed. The input values for $x_\pm$ and $y_\pm$ are set close to those determined by previous measurements [42]. The uncertainties estimated by the fit are consistent with the size of the uncertainties estimated by the pseudo-experiments. However, small biases, with sizes around 10% of the statistical uncertainty, are observed in the central values. These biases are due to the low event yields in some of the bins and are observed to reduce in simulated experiments of larger size. The central values are corrected for the biases.

The results of the fits are presented in Table 3. The statistical uncertainties are compatible with those predicted by the simulated pseudo-experiments. The systematic uncertainties are discussed in Sect. 8. The inclusion of $D \to K^0_S K^+ K^-$ data improves the precision on $x_\pm$ by around 10% and by a smaller amount for $y_\pm$. This is expected, as the measured values of c_i in this decay, which multiply $x_\pm$ in Eq. 3, are significantly larger than those of s_i, which multiply $y_\pm$ [18].

The measured values of $(x_\pm, y_\pm)$ from the fit to all data, with their likelihood contours corresponding to statistical uncertainties only, are displayed in Fig. 9. The expected signature for a sample that exhibits *CP* violation is that the two vectors defined by the coordinates (x_-, y_-) and (x_+, y_+) should both be non-zero in magnitude and have a non-zero opening angle, which is equal to 2γ.

To investigate whether the binned fit gives an adequate description of the data, a study is performed to compare the expected signal yield in each bin, given by the fitted total yield and the values of $x_\pm$ and $y_\pm$, and the observed number of signal candidates

Table 3: Results for $x_\pm$ and $y_\pm$ from fits of both the $D \to K^0_S\pi^+\pi^-$ and $D \to K^0_S K^+K^-$ samples, and from fits of the $D \to K^0_S\pi^+\pi^-$ sample only. The first, second, and third uncertainties are the statistical, the experimental systematic, and the error associated with the precision of the strong-phase parameters, respectively.

Parameter	All data	$D \to K^0_S\pi^+\pi^-$ only
x_+ $[\times 10^{-2}]$	$-7.7 \pm 2.4 \pm 1.0 \pm 0.4$	$-7.5 \pm 2.7 \pm 1.1 \pm 0.5$
x_- $[\times 10^{-2}]$	$2.5 \pm 2.5 \pm 1.0 \pm 0.5$	$2.6 \pm 2.8 \pm 1.1 \pm 0.7$
y_+ $[\times 10^{-2}]$	$-2.2 \pm 2.5 \pm 0.4 \pm 1.0$	$-1.4 \pm 2.6 \pm 0.6 \pm 0.9$
y_- $[\times 10^{-2}]$	$7.5 \pm 2.9 \pm 0.5 \pm 1.4$	$7.5 \pm 3.0 \pm 0.4 \pm 1.5$

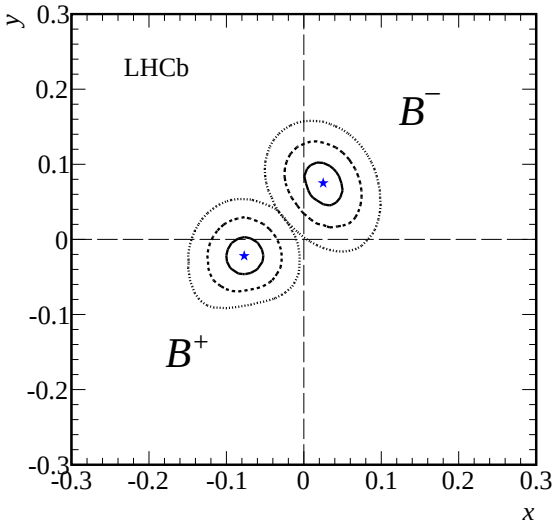

Figure 9: Confidence levels at 39.3%, 86.5% and 98.9% probability for (x_+, y_+) and (x_-, y_-) as measured in $B^\pm \to DK^\pm$ decays (statistical uncertainties only). The parameters (x_+, y_+) relate to B^+ decays and (x_-, y_-) refer to B^- decays. The stars represent the best fit central values.

in each bin. The latter is determined by fitting directly in each bin for the $B^\pm \to DK^\pm$ candidate yield. This study is performed using effective bin numbers and with long and downstream K^0_S decays combined. Figure 10 shows the results separately for the sum of B^+ and B^- candidates, $N_{B^+} + N_{B^-}$, and for the difference, $N_{B^+} - N_{B^-}$, which is sensitive to *CP* violation. The expected signal yields assuming *CP* symmetry ($x_\pm = y_\pm = 0$) in the $N_{B^+} - N_{B^-}$ distribution are also shown. These are not constant at $N_{B^+} - N_{B^-} = 0$ because they are calculated using the total B^+ and B^- yields, which do not have identical values. The data and fit expectations are compatible for both distributions yielding a χ^2 probability (p-value) of 93% for $N_{B^+} + N_{B^-}$ and 80% for $N_{B^+} - N_{B^-}$. The results for the $N_{B^+} - N_{B^-}$ distribution are less compatible with the hypothesis of *CP* symmetry, which has a p-value of 4%.

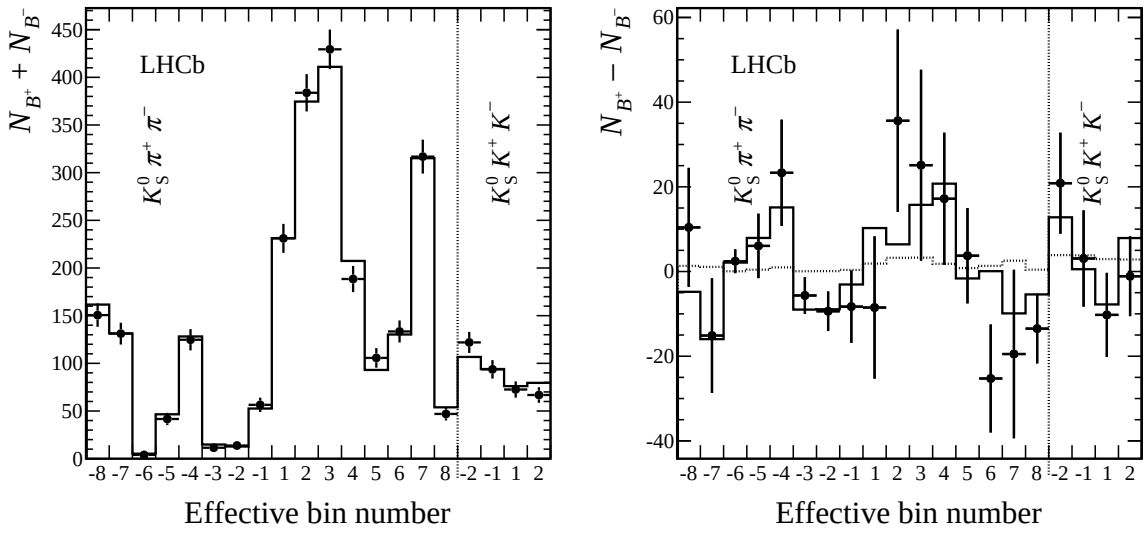

Figure 10: Combinations of signal yields (data points) in effective bins compared with prediction of $(x_\pm, y_\pm)$ fit (solid histogram) for $D \to K^0_S\pi^+\pi^-$ and $D \to K^0_S K^+K^-$ decays. The dotted histograms give the prediction for $x_\pm = y_\pm = 0$. The left plot shows the sum of B^+ and B^- yields and the right plot shows the difference of B^+ and B^- yields.

Table 4: Summary of statistical, experimental, and strong-phase, uncertainties on $x_\pm$ and $y_\pm$ in the case where both $D \to K^0_S\pi^+\pi^-$ and $D \to K^0_S K^+K^-$ decays are included in the fit. All entries are given in multiples of 10^{-2}.

Source	$\sigma(x_+)$	$\sigma(x_-)$	$\sigma(y_+)$	$\sigma(y_-)$
Statistical	2.4	2.5	2.5	2.9
Efficiency corrections	0.9	0.9	0.2	0.2
Mass fit PDFs	0.2	0.2	0.1	0.2
Shape of $D\pi^\pm$ mis-identified as $DK^\pm$	0.1	0.1	0.0	0.1
Shape of partially reconstructed backgrounds	0.1	0.3	0.1	0.2
c_i, s_i bias due to efficiency	0.0	0.0	0.1	0.0
Migration	0.1	0.1	0.2	0.2
Bias correction	0.2	0.2	0.2	0.2
Total experimental	1.0	1.0	0.4	0.5
Strong-phase-related uncertainties	0.4	0.5	1.0	1.4

8 Systematic uncertainties

Systematic uncertainties are evaluated for the fits to the full data sample and are presented in Table 4. The uncertainties arising from the CLEO-c measurements are kept separate from the other experimental uncertainties.

A systematic uncertainty arises due to the mismodelling in the simulation used to

derive the efficiency correction used in the determination of the F_i parameters. To determine the systematic uncertainty associated with this correction, an alternative set of correction factors is calculated and used to evaluate an alternative set of F_i parameters. The alternative correction factors are calculated by incorporating an extra term (Eq. 10) determined from a new rectangular binning scheme, as shown in Fig. 11. The bin-to-bin efficiency variation in this rectangular scheme is significantly larger than for the default partitioning and is more sensitive to imperfections in the simulated data efficiency profile. The bin sizes are chosen to keep the expected yields in each bin as similar as possible. The yields of the $B^\pm \to D\pi^\pm$ and $\overline{B}^{(}{}^{)} \to D^{*\pm}\mu^{\mp(}\overline{\nu}^{)}_{\mu}$ decays in each bin of the rectangular scheme are compared to the predictions from the amplitude model and the simulated data efficiency profile. Differences of up to 15% are observed. These differences are consistent for the two decay modes. The alternative correction factors, $\xi_i^{\rm alt}$, are calculated using the following equation:

$$\xi_i^{\rm alt} = \frac{\int_{\mathcal{D}_i} \varepsilon_{DK}\,|A|^2\,C_{D\pi}\,d\mathcal{D}}{\int_{\mathcal{D}_i} \varepsilon_{D^*\mu}\,|A|^2\,C_{D^*\mu}\,d\mathcal{D}} \tag{10}$$

where the $C = C(m_-^2, m_+^2)$ terms are the ratios between the predicted and observed data yields in the rectangular binning. Many pseudo-experiments are performed in which the data are generated according to the default F_i but are fitted assuming that the alternative F_i set are true. The overall shift in the fitted values of the *CP* parameters in comparison to their input values is taken as the systematic uncertainty, yielding 0.9×10^{-2} for $x_\pm$ and 0.2×10^{-2} for $y_\pm$.

To assign an uncertainty for the imperfections in the description of the invariant mass spectrum, three changes to the model are considered. Firstly, an alternate signal shape is considered that has wider resolution and longer tails. This alternate shape uses a different form of modified Gaussian and the parameters are derived from a fit to data. Secondly, the description of the partially reconstructed background is changed to a shape obtained from a fit of the PDF to simulated $D \to K^0_{\rm S}h^+h^-$ decays. Finally, the parameters of the misidentified background PDF are changed to vary the tail under the signal peak as this is the part of the PDF that is least well determined. For each change, the effects on the *CP* parameters are determined using many pseudo-experiments where the data are generated with the default PDFs and fitted with the alternate models. The contributions from each change are summed in quadrature and are $(0.1\text{–}0.2) \times 10^{-2}$.

Two systematic uncertainties are evaluated that are associated with the misidentified $B^\pm \to D\pi^\pm$ background in the $B^\pm \to DK^\pm$ sample. The uncertainties on the particle misidentification efficiencies are found to have a negligible effect on the measured values of $x_\pm$ and $y_\pm$. It is possible that the invariant mass distribution of the misidentified background is not uniform over the Dalitz plot, as is assumed in the fit. This can occur through kinematic correlations between the reconstruction efficiency on the Dalitz plot of the D decay and the momentum of the bachelor pion from the $B^\pm$ decay. Pseudo-experiments are performed with different mass shapes input according to the Dalitz plot bin and the results of simulation studies. These experiments are then fitted assuming a uniform shape, as in data. The resulting uncertainty is up to 0.1×10^{-2} for all *CP*

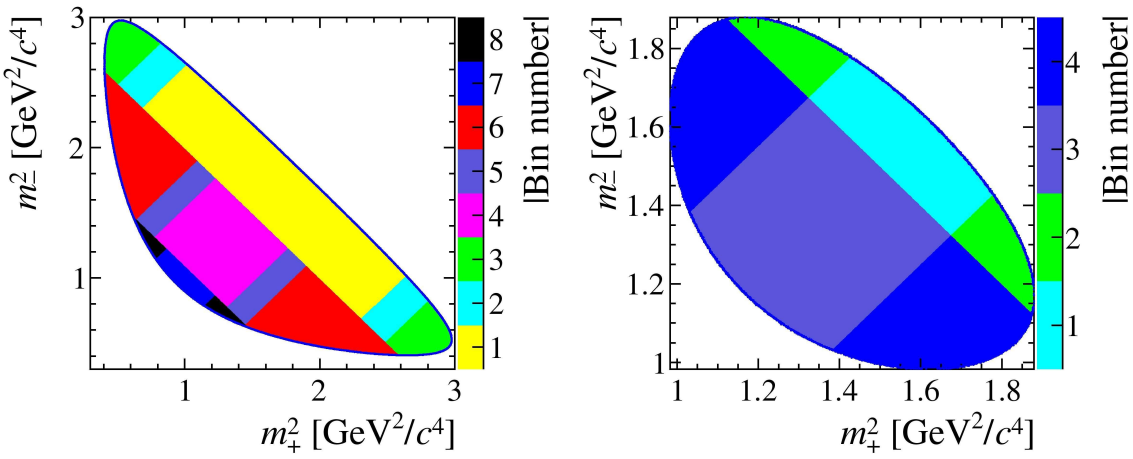

Figure 11: The rectangular binning schemes for the two decays. On the left (right) is plotted the scheme for the $K^0_S\pi^+\pi^-$ ($K^0_S K^+K^-$) decay.

parameters.

The distribution of the partially reconstructed background is varied over the Dalitz plot according to the uncertainty in the composition of this background component. This results in a different invariant mass distribution in each Dalitz plot bin. An uncertainty of (0.1–0.3) $\times 10^{-2}$ is assigned to the fitted parameters in the full data fit.

The non-uniform efficiency profile over the Dalitz plot means that the values of (c_i, s_i) appropriate for this analysis can differ from those measured at CLEO-c, which correspond to the constant efficiency case. This leads to a potential bias in the determination of $x_\pm$ and $y_\pm$. The possible size of this effect is evaluated using the LHCb simulation. The Dalitz plot bins are divided into smaller cells, and the BaBar amplitude model [10, 11] is used to calculate the values of c_i and s_i within each cell. These values are then averaged together and weighted by the population of each cell after efficiency losses to obtain an effective (c_i, s_i) for the bin as a whole. The results are compared with those determined assuming a constant efficiency; the differences between the two sets of results are found to be small compared with the CLEO-c measurement uncertainties. The data are fitted multiple times, each with different (c_i, s_i) values sampled according to the size of these differences, and the mean shifts are assigned as a systematic uncertainty. These shifts are less than 0.1×10^{-2} for all CP parameters.

For both $B^\pm \to DK^\pm$ and $\overline{(B)} \to D^{*\pm}\mu^{\mp}\overline{(\nu)}_\mu$ decays the resolution in m^2_+ and m^2_- of each decay is approximately $0.005\,\text{GeV}^2/c^4$ for candidates with long K^0_S decays and $0.006\,\text{GeV}^2/c^4$ for candidates with downstream K^0_S. This is small compared to the typical width of a bin but net migration away from the more densely populated bins is possible. To first order this effect is accounted for by use of the control channel, but residual effects enter due to the different distribution in the Dalitz plot of the signal events. The uncertainty due to these residual effects is determined via pseudo-experiments, in which different input F_i values are used to reflect the residual migration. The size of any possible bias is found

Table 5: Correlation matrix between the $x_\pm$, $y_\pm$ parameters for the full data set.

	x_+	x_-	y_+	y_-
x_+	1.000	0.027	0.003	−0.007
x_-		1.000	0.009	−0.200
y_+			1.000	−0.016
y_-				1.000

to vary between 0.1×10^{-2} and 0.2×10^{-2}.

An uncertainty is assigned to each *CP* parameter to accompany the correction that is applied for the small bias observed in the fit procedure. These uncertainties are determined by performing sets of pseudo-experiments, each generated with different values of $x_\pm$ and $y_\pm$ according to the range allowed by current experimental knowledge. The spread in observed bias is combined in quadrature with half the correction and the uncertainty in the precision of the pseudo-experiments. This is taken as the systematic uncertainty, and is 0.2×10^{-2} for all *CP* parameters. The effect that a detection asymmetry between hadrons of opposite charge can have on the symmetry of the efficiency of the Dalitz plot is found to be negligible. Changes in the mass model used to describe the semileptonic control sample are found to have a negligible effect on the F_i values.

The limited precision on (c_i, s_i) coming from the CLEO-c measurement induces uncertainties on $x_\pm$ and $y_\pm$ [18]. These uncertainties are evaluated by fitting the data multiple times, each with different (c_i, s_i) values sampled according to their experimental uncertainties and correlations. The resulting width in the distribution of $x_\pm, y_\pm$ values is assigned as the systematic uncertainty. Values of $(0.4\text{–}1.4) \times 10^{-2}$ are found for the fit to the full sample. The uncertainties are smaller than those reported in Ref. [4]. This is as expected since it is found from simulation studies that the $(c_i,\ s_i)$ uncertainty also depends on the sample size.

Finally, several checks are conducted to assess the stability of the results. These include repeating the fits separately for both K^0_S categories, for the centre-of-mass energy at which the data were collected, and for candidates passing different hardware trigger requirements. No anomalies are found, and no additional systematic uncertainties are assigned.

The total experimental systematic uncertainty from LHCb-related sources is determined to be 1.0×10^{-2} on x_+, 1.0×10^{-2} on x_-, 0.4×10^{-2} on y_+, and 0.5×10^{-2} on y_-. These are all smaller than the corresponding statistical uncertainties. The dominant contribution arises from the efficiency correction method.

After taking account of all sources of uncertainty the correlation matrix between the measured $x_\pm$, $y_\pm$ parameters for the full data set is shown in Table 5. Correlations from the statistical and strong-phase uncertainties are included but the experimental systematic uncertainties are treated as uncorrelated. The equivalent matrix for $D \to K^0_S\pi^+\pi^-$ decays only is shown in Table 6.

The systematic uncertainties for the case where only $D \to K^0_S\pi^+\pi^-$ decays are included

Table 6: Correlation matrix between the $x_\pm$, $y_\pm$ parameters for $K^0_S\pi^+\pi^-$ decays only.

	x_+	x_-	y_+	y_-
x_+	1.000	0.017	−0.038	−0.008
x_-		1.000	0.009	−0.220
y_+			1.000	0.004
y_-				1.000

are also given in Table 3. The total experimental systematic in this case is larger and this is primarily driven by a larger systematic effect due to the simulation-derived efficiency correction, for which the systematic uncertainty for the $D \to K^0_S K^+ K^-$ decays partially compensates. The uncertainties due to the CLEO-c strong-phase measurements are also slightly larger when considering only $D \to K^0_S\pi^+\pi^-$ decays due to the dependence of this systematic uncertainty on the signal sample and its size.

9 Results and interpretation

The results for $x_\pm$ and $y_\pm$ can be interpreted in terms of the underlying physics parameters γ, r_B and δ_B. This interpretation is performed using a frequentist approach with Feldman-Cousins ordering [43], using the same procedure as described in Ref. [19], yielding confidence levels for the three physics parameters.

In Fig. 12 the projections of the three-dimensional surfaces bounding the one, two and three standard deviation volumes onto the (γ, r_B) and (γ, δ_B) planes are shown. The LHCb-related systematic uncertainties are taken as uncorrelated and correlations of the CLEO-c and statistical uncertainties are taken into account. The statistical and systematic uncertainties on $x_\pm$ and $y_\pm$ are combined in quadrature.

The solution for the physics parameters has a two-fold ambiguity: $(\gamma, \delta_B) \to (\gamma + 180^\circ, \delta_B + 180^\circ)$. Choosing the solution that satisfies $0 < \gamma < 180^\circ$ yields $r_B = 0.080^{+0.019}_{-0.021}$, $\gamma = (62^{+15}_{-14})^\circ$ and $\delta_B = (134^{+14}_{-15})^\circ$. The values for γ and r_B are consistent with the world average of results from previous experiments [42]. The significant increase in precision compared to the measurement in Ref. [4] is due to a combination of increased signal yield, lower systematic uncertainties and a higher central value for r_B.

10 Conclusions

Approximately 2580 $B^\pm \to DK^\pm$ decays, with the D meson decaying either to $K^0_S\pi^+\pi^-$ or $K^0_S K^+ K^-$, are selected from data corresponding to and integrated luminosity of 3.0 fb^{-1} collected by LHCb in 2011 and 2012. These samples are analysed to determine the CP-violating parameters $x_\pm \equiv r_B \cos(\delta_B \pm \gamma)$ and $y_\pm \equiv r_B \sin(\delta_B \pm \gamma)$, where r_B is the ratio of the absolute values of the $B^+ \to D^0 K^-$ and $B^+ \to \overline{D}^0 K^-$ amplitudes, δ_B is the

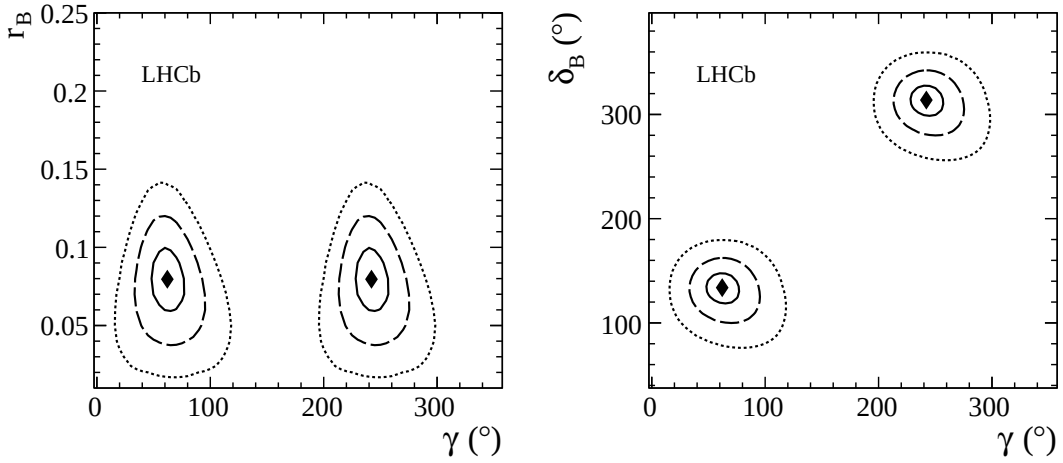

Figure 12: The three-dimensional confidence volumes, corresponding to 19.9%, 73.9% and 97.1% confidence levels, are projected onto the (γ, r_B) and (γ, δ_B) planes. The confidence levels are given by solid, dashed and dotted contours. The diamonds mark the central values.

strong-phase difference between them, and γ is an angle of the unitarity triangle. The analysis is performed in bins of the D decay Dalitz plot, and existing measurements of the CLEO-c experiment are used to provide input on the D decay strong-phase parameters (c_i, s_i) [18]. Such an approach allows the analysis to be free from any model-dependent assumptions on the strong-phase variation across the Dalitz plot. The following results are obtained:

$$x_+ = (-7.7 \pm 2.4 \pm 1.0 \pm 0.4) \times 10^{-2}, \qquad x_- = (2.5 \pm 2.5 \pm 1.0 \pm 0.5) \times 10^{-2},$$
$$y_+ = (-2.2 \pm 2.5 \pm 0.4 \pm 1.0) \times 10^{-2}, \qquad y_- = (7.5 \pm 2.9 \pm 0.5 \pm 1.4) \times 10^{-2},$$

where the first uncertainties are statistical, the second are systematic and the third arise from the experimental knowledge of the (c_i, s_i) parameters. The results are the most precise values of these *CP* observables obtained from a single measurement.

From the above results, the following values of the underlying physics parameters are derived: $r_B = 0.080^{+0.019}_{-0.021}$, $\gamma = (62^{+15}_{-14})^\circ$ and $\delta_B = (134^{+14}_{-15})^\circ$. These values are consistent with the world averages of results from previous measurements [20], but should not be combined with the model-dependent measurements [15]. These values improve upon and supersede the results from a previous model-independent measurement performed with 1.0 fb^{-1} of data collected by LHCb in 2011 [4].

Acknowledgements

We express our gratitude to our colleagues in the CERN accelerator departments for the excellent performance of the LHC. We thank the technical and administrative staff at the

LHCb institutes. We acknowledge support from CERN and from the national agencies: CAPES, CNPq, FAPERJ and FINEP (Brazil); NSFC (China); CNRS/IN2P3 (France); BMBF, DFG, HGF and MPG (Germany); SFI (Ireland); INFN (Italy); FOM and NWO (The Netherlands); MNiSW and NCN (Poland); MEN/IFA (Romania); MinES and FANO (Russia); MinECo (Spain); SNSF and SER (Switzerland); NASU (Ukraine); STFC (United Kingdom); NSF (USA). The Tier1 computing centres are supported by IN2P3 (France), KIT and BMBF (Germany), INFN (Italy), NWO and SURF (The Netherlands), PIC (Spain), GridPP (United Kingdom). We are indebted to the communities behind the multiple open source software packages on which we depend. We are also thankful for the computing resources and the access to software R&D tools provided by Yandex LLC (Russia). Individual groups or members have received support from EPLANET, Marie Skłodowska-Curie Actions and ERC (European Union), Conseil général de Haute-Savoie, Labex ENIGMASS and OCEVU, Région Auvergne (France), RFBR (Russia), XuntaGal and GENCAT (Spain), Royal Society and Royal Commission for the Exhibition of 1851 (United Kingdom).

References

[1] LHCb collaboration, R. Aaij *et al.*, *Observation of CP violation in $B^\pm \to DK^\pm$ decays*, Phys. Lett. **B712** (2012) 203, Erratum ibid. **B713** (2012) 351, arXiv:1203.3662.

[2] LHCb collaboration, R. Aaij *et al.*, *Observation of the suppressed ADS modes $B^\pm \to [\pi^\pm K^\mp \pi^+ \pi^-]_D K^\pm$ and $B^\pm \to [\pi^\pm K^\mp \pi^+ \pi^-]_D \pi^\pm$*, Phys. Lett. **B723** (2013) 44, arXiv:1303.4646.

[3] LHCb collaboration, R. Aaij *et al.*, *A study of CP violation in $B^\pm \to DK^\pm$ and $B^\pm \to D\pi^\pm$ decays with $D \to K^0_S K^\pm \pi^\mp$ final states*, Phys. Lett. **B733** (2014) 36, arXiv:1402.2982.

[4] LHCb collaboration, R. Aaij *et al.*, *A model-independent Dalitz plot analysis of $B^\pm \to DK^\pm$ with $D \to K^0_S h^+ h^-$ ($h = \pi, K$) decays and constraints on the CKM angle γ*, Phys. Lett. **B718** (2012) 43, arXiv:1209.5869.

[5] LHCb collaboration, R. Aaij *et al.*, *Measurements of CP violation parameters in $B^0 \to DK^{*0}$ decays*, arXiv:1407.8136, submitted to Phys. Rev. D.

[6] LHCb collaboration, R. Aaij *et al.*, *Measurement of CP asymmetry in $B^0_s \to D^\mp_s K^\pm$ decays*, arXiv:1407.6127, submitted to JHEP.

[7] A. Giri, Y. Grossman, A. Soffer, and J. Zupan, *Determining γ using $B^\pm \to DK^\pm$ with multibody D decays*, Phys. Rev. **D68** (2003) 054018, arXiv:hep-ph/0303187.

[8] A. Bondar, *Proceedings of BINP special analysis meeting on Dalitz analysis, 24-26 Sep. 2002, unpublished.*

[9] BaBar collaboration, B. Aubert *et al.*, *Measurement of the Cabibbo-Kobayashi-Maskawa angle γ in $B^\mp \to D^{(*)} K^\mp$ decays with a Dalitz analysis of $D \to K^0_S \pi^- \pi^+$*, Phys. Rev. Lett. **95** (2005) 121802, arXiv:hep-ex/0504039.

[10] BaBar collaboration, B. Aubert *et al.*, *Improved measurement of the CKM angle γ in $B^\mp \to D^{(*)} K^{(*\mp)}$ decays with a Dalitz plot analysis of D decays to $K^0_S \pi^+ \pi^-$ and $K^0_S K^+ K^-$*, Phys. Rev. **D78** (2008) 034023, arXiv:0804.2089.

[11] BaBar collaboration, P. del Amo Sanchez *et al.*, *Evidence for direct CP violation in the measurement of the Cabibbo-Kobayashi-Maskawa angle γ with $B^\mp \to D^{(*)} K^{(*)\mp}$ decays*, Phys. Rev. Lett. **105** (2010) 121801, arXiv:1005.1096.

[12] Belle collaboration, A. Poluektov *et al.*, *Measurement of ϕ_3 with Dalitz plot analysis of $B^\pm \to D^{(*)} K^\pm$ decay*, Phys. Rev. **D70** (2004) 072003, arXiv:hep-ex/0406067.

[13] Belle collaboration, A. Poluektov *et al.*, *Measurement of ϕ_3 with Dalitz plot analysis of $B^+ \to D^{(*)} K^{(*)+}$ decay*, Phys. Rev. **D73** (2006) 112009, arXiv:hep-ex/0604054.

[14] Belle collaboration, A. Poluektov *et al.*, *Evidence for direct CP violation in the decay $B \to D^{(*)}K$, $D \to K^0_S\pi^+\pi^-$ and measurement of the CKM phase ϕ_3*, Phys. Rev. **D81** (2010) 112002, arXiv:1003.3360.

[15] LHCb collaboration, R. Aaij *et al.*, *Measurement of CP violation and constraints on the CKM angle γ in $B^\pm \to DK^\pm$ with $D \to K^0_S\pi^+\pi^-$ decays*, arXiv:1407.6211, submitted to Nucl. Phys. B.

[16] A. Bondar and A. Poluektov, *Feasibility study of model-independent approach to ϕ_3 measurement using Dalitz plot analysis*, Eur. Phys. J. **C47** (2006) 347, arXiv:hep-ph/0510246.

[17] A. Bondar and A. Poluektov, *The use of quantum-correlated D^0 decays for ϕ_3 measurement*, Eur. Phys. J. **C55** (2008) 51, arXiv:0801.0840.

[18] CLEO collaboration, J. Libby *et al.*, *Model-independent determination of the strong-phase difference between D^0 and $\overline{D}^0 \to K^0_{S,L}h^+h^-$ ($h = \pi, K$) and its impact on the measurement of the CKM angle γ/ϕ_3*, Phys. Rev. **D82** (2010) 112006, arXiv:1010.2817.

[19] Belle collaboration, H. Aihara *et al.*, *First measurement of ϕ_3 with a model-independent Dalitz plot analysis of $B^\pm \to DK^\pm$, $D \to K^0_S\pi^+\pi^-$ decay*, Phys. Rev. **D85** (2012) 112014, arXiv:1204.6561.

[20] Particle Data Group, J. Beringer *et al.*, *Review of particle physics*, Phys. Rev. **D86** (2012) 010001, and 2013 partial update for the 2014 edition.

[21] A. Bondar, A. Poluektov, and V. Vorobiev, *Charm mixing in a model-independent analysis of correlated $D^0\overline{D}^0$ decays*, Phys. Rev. **D82** (2010) 034033, arXiv:1004.2350.

[22] Y. Grossman and M. Savastio, *Effects of K^0–$\overline{K}^0$ mixing on determining γ from $B^\pm \to DK^\pm$*, JHEP **03** (2014) 008, arXiv:1311.3575.

[23] LHCb collaboration, R. Aaij *et al.*, *Measurement of CP asymmetry in $D^0 \to K^-K^+$ and $D^0 \to \pi^-\pi^+$ decays*, JHEP **07** (2014) 041, arXiv:1405.2797.

[24] LHCb collaboration, A. A. Alves Jr. *et al.*, *The LHCb detector at the LHC*, JINST **3** (2008) S08005.

[25] R. Arink *et al.*, *Performance of the LHCb Outer Tracker*, JINST **9** (2014) P01002, arXiv:1311.3893.

[26] M. Adinolfi *et al.*, *Performance of the LHCb RICH detector at the LHC*, Eur. Phys. J. **C73** (2013) 2431, arXiv:1211.6759.

[27] A. A. Alves Jr. *et al.*, *Performance of the LHCb muon system*, JINST **8** (2013) P02022, arXiv:1211.1346.

[28] R. Aaij *et al.*, *The LHCb trigger and its performance in 2011*, JINST **8** (2013) P04022, arXiv:1211.3055.

[29] T. Sjöstrand, S. Mrenna, and P. Skands, *PYTHIA 6.4 physics and manual*, JHEP **05** (2006) 026, arXiv:hep-ph/0603175.

[30] T. Sjöstrand, S. Mrenna, and P. Skands, *A brief introduction to PYTHIA 8.1*, Comput. Phys. Commun. **178** (2008) 852, arXiv:0710.3820.

[31] I. Belyaev *et al.*, *Handling of the generation of primary events in* Gauss*, the LHCb simulation framework*, Nuclear Science Symposium Conference Record (NSS/MIC) **IEEE** (2010) 1155.

[32] D. J. Lange, *The EvtGen particle decay simulation package*, Nucl. Instrum. Meth. **A462** (2001) 152.

[33] P. Golonka and Z. Was, *PHOTOS Monte Carlo: a precision tool for QED corrections in Z and W decays*, Eur. Phys. J. **C45** (2006) 97, arXiv:hep-ph/0506026.

[34] Geant4 collaboration, J. Allison *et al.*, *Geant4 developments and applications*, IEEE Trans. Nucl. Sci. **53** (2006) 270.

[35] Geant4 collaboration, S. Agostinelli *et al.*, *Geant4: a simulation toolkit*, Nucl. Instrum. Meth. **A506** (2003) 250.

[36] M. Clemencic *et al.*, *The LHCb simulation application,* Gauss*: design, evolution and experience*, J. Phys. Conf. Ser. **331** (2011) 032023.

[37] V. V. Gligorov and M. Williams, *Efficient, reliable and fast high-level triggering using a bonsai boosted decision tree*, JINST **8** (2013) P02013, arXiv:1210.6861.

[38] L. Breiman, J. H. Friedman, R. A. Olshen, and C. J. Stone, *Classification and regression trees*, Wadsworth international group, Belmont, California, USA, 1984.

[39] R. E. Schapire and Y. Freund, *A decision-theoretic generalization of on-line learning and an application to boosting*, Jour. Comp. and Syst. Sc. **55** (1997) 119.

[40] W. D. Hulsbergen, *Decay chain fitting with a Kalman filter*, Nucl. Instrum. Meth. **A552** (2005) 566, arXiv:physics/0503191.

[41] M. Pivk and F. R. Le Diberder, *sPlot: a statistical tool to unfold data distributions*, Nucl. Instrum. Meth. **A555** (2005) 356, arXiv:physics/0402083.

[42] Heavy Flavor Averaging Group, D. Asner *et al.*, *Averages of b-hadron, c-hadron, and τ-lepton properties*, arXiv:1010.1589, Updates available online at http://www.slac.stanford.edu/xorg/hfag.

[43] G. J. Feldman and R. D. Cousins, *A unified approach to the classical statistical analysis of small signals*, Phys. Rev. **D57** (1998) 3873, arXiv:physics/9711021.

LHCb collaboration

R. Aaij[41], B. Adeva[37], M. Adinolfi[46], A. Affolder[52], Z. Ajaltouni[5], S. Akar[6], J. Albrecht[9], F. Alessio[38], M. Alexander[51], S. Ali[41], G. Alkhazov[30], P. Alvarez Cartelle[37], A.A. Alves Jr[25,38], S. Amato[2], S. Amerio[22], Y. Amhis[7], L. An[3], L. Anderlini[17,g], J. Anderson[40], R. Andreassen[57], M. Andreotti[16,f], J.E. Andrews[58], R.B. Appleby[54], O. Aquines Gutierrez[10], F. Archilli[38], A. Artamonov[35], M. Artuso[59], E. Aslanides[6], G. Auriemma[25,n], M. Baalouch[5], S. Bachmann[11], J.J. Back[48], A. Badalov[36], W. Baldini[16], R.J. Barlow[54], C. Barschel[38], S. Barsuk[7], W. Barter[47], V. Batozskaya[28], V. Battista[39], A. Bay[39], L. Beaucourt[4], J. Beddow[51], F. Bedeschi[23], I. Bediaga[1], S. Belogurov[31], K. Belous[35], I. Belyaev[31], E. Ben-Haim[8], G. Bencivenni[18], S. Benson[38], J. Benton[46], A. Berezhnoy[32], R. Bernet[40], M.-O. Bettler[47], M. van Beuzekom[41], A. Bien[11], S. Bifani[45], T. Bird[54], A. Bizzeti[17,i], P.M. Bjørnstad[54], T. Blake[48], F. Blanc[39], J. Blouw[10], S. Blusk[59], V. Bocci[25], A. Bondar[34], N. Bondar[30,38], W. Bonivento[15,38], S. Borghi[54], A. Borgia[59], M. Borsato[7], T.J.V. Bowcock[52], E. Bowen[40], C. Bozzi[16], T. Brambach[9], J. van den Brand[42], J. Bressieux[39], D. Brett[54], M. Britsch[10], T. Britton[59], J. Brodzicka[54], N.H. Brook[46], H. Brown[52], A. Bursche[40], G. Busetto[22,r], J. Buytaert[38], S. Cadeddu[15], R. Calabrese[16,f], M. Calvi[20,k], M. Calvo Gomez[36,p], P. Campana[18,38], D. Campora Perez[38], A. Carbone[14,d], G. Carboni[24,l], R. Cardinale[19,38,j], A. Cardini[15], L. Carson[50], K. Carvalho Akiba[2], G. Casse[52], L. Cassina[20], L. Castillo Garcia[38], M. Cattaneo[38], Ch. Cauet[9], R. Cenci[58], M. Charles[8], Ph. Charpentier[38], M. Chefdeville[4], S. Chen[54], S.-F. Cheung[55], N. Chiapolini[40], M. Chrzaszcz[40,26], K. Ciba[38], X. Cid Vidal[38], G. Ciezarek[53], P.E.L. Clarke[50], M. Clemencic[38], H.V. Cliff[47], J. Closier[38], V. Coco[38], J. Cogan[6], E. Cogneras[5], L. Cojocariu[29], P. Collins[38], A. Comerma-Montells[11], A. Contu[15], A. Cook[46], M. Coombes[46], S. Coquereau[8], G. Corti[38], M. Corvo[16,f], I. Counts[56], B. Couturier[38], G.A. Cowan[50], D.C. Craik[48], M. Cruz Torres[60], S. Cunliffe[53], R. Currie[50], C. D'Ambrosio[38], J. Dalseno[46], P. David[8], P.N.Y. David[41], A. Davis[57], K. De Bruyn[41], S. De Capua[54], M. De Cian[11], J.M. De Miranda[1], L. De Paula[2], W. De Silva[57], P. De Simone[18], D. Decamp[4], M. Deckenhoff[9], L. Del Buono[8], N. Déléage[4], D. Derkach[55], O. Deschamps[5], F. Dettori[38], A. Di Canto[38], H. Dijkstra[38], S. Donleavy[52], F. Dordei[11], M. Dorigo[39], A. Dosil Suárez[37], D. Dossett[48], A. Dovbnya[43], K. Dreimanis[52], G. Dujany[54], F. Dupertuis[39], P. Durante[38], R. Dzhelyadin[35], A. Dziurda[26], A. Dzyuba[30], S. Easo[49,38], U. Egede[53], V. Egorychev[31], S. Eidelman[34], S. Eisenhardt[50], U. Eitschberger[9], R. Ekelhof[9], L. Eklund[51], I. El Rifai[5], Ch. Elsasser[40], S. Ely[59], S. Esen[11], H.-M. Evans[47], T. Evans[55], A. Falabella[14], C. Färber[11], C. Farinelli[41], N. Farley[45], S. Farry[52], RF Fay[52], D. Ferguson[50], V. Fernandez Albor[37], F. Ferreira Rodrigues[1], M. Ferro-Luzzi[38], S. Filippov[33], M. Fiore[16,f], M. Fiorini[16,f], M. Firlej[27], C. Fitzpatrick[39], T. Fiutowski[27], M. Fontana[10], F. Fontanelli[19,j], R. Forty[38], O. Francisco[2], M. Frank[38], C. Frei[38], M. Frosini[17,38,g], J. Fu[21,38], E. Furfaro[24,l], A. Gallas Torreira[37], D. Galli[14,d], S. Gallorini[22], S. Gambetta[19,j], M. Gandelman[2], P. Gandini[59], Y. Gao[3], J. García Pardiñas[37], J. Garofoli[59], J. Garra Tico[47], L. Garrido[36], C. Gaspar[38], R. Gauld[55], L. Gavardi[9], G. Gavrilov[30], A. Geraci[21,v], E. Gersabeck[11], M. Gersabeck[54], T. Gershon[48], Ph. Ghez[4], A. Gianelle[22], S. Giani'[39], V. Gibson[47], L. Giubega[29], V.V. Gligorov[38], C. Göbel[60], D. Golubkov[31], A. Golutvin[53,31,38], A. Gomes[1,a], C. Gotti[20], M. Grabalosa Gándara[5], R. Graciani Diaz[36], L.A. Granado Cardoso[38], E. Graugés[36], G. Graziani[17], A. Grecu[29], E. Greening[55], S. Gregson[47], P. Griffith[45], L. Grillo[11], O. Grünberg[62], B. Gui[59], E. Gushchin[33], Yu. Guz[35,38], T. Gys[38], C. Hadjivasiliou[59], G. Haefeli[39], C. Haen[38], S.C. Haines[47], S. Hall[53], B. Hamilton[58], T. Hampson[46], X. Han[11], S. Hansmann-Menzemer[11], N. Harnew[55], S.T. Harnew[46], J. Harrison[54],

J. He[38], T. Head[38], V. Heijne[41], K. Hennessy[52], P. Henrard[5], L. Henry[8], J.A. Hernando Morata[37], E. van Herwijnen[38], M. Heß[62], A. Hicheur[1], D. Hill[55], M. Hoballah[5], C. Hombach[54], W. Hulsbergen[41], P. Hunt[55], N. Hussain[55], D. Hutchcroft[52], D. Hynds[51], M. Idzik[27], P. Ilten[56], R. Jacobsson[38], A. Jaeger[11], J. Jalocha[55], E. Jans[41], P. Jaton[39], A. Jawahery[58], F. Jing[3], M. John[55], D. Johnson[55], C.R. Jones[47], C. Joram[38], B. Jost[38], N. Jurik[59], M. Kaballo[9], S. Kandybei[43], W. Kanso[6], M. Karacson[38], T.M. Karbach[38], S. Karodia[51], M. Kelsey[59], I.R. Kenyon[45], T. Ketel[42], B. Khanji[20], C. Khurewathanakul[39], S. Klaver[54], K. Klimaszewski[28], O. Kochebina[7], M. Kolpin[11], I. Komarov[39], R.F. Koopman[42], P. Koppenburg[41,38], M. Korolev[32], A. Kozlinskiy[41], L. Kravchuk[33], K. Kreplin[11], M. Kreps[48], G. Krocker[11], P. Krokovny[34], F. Kruse[9], W. Kucewicz[26,o], M. Kucharczyk[20,26,38,k], V. Kudryavtsev[34], K. Kurek[28], T. Kvaratskheliya[31], V.N. La Thi[39], D. Lacarrere[38], G. Lafferty[54], A. Lai[15], D. Lambert[50], R.W. Lambert[42], G. Lanfranchi[18], C. Langenbruch[48], B. Langhans[38], T. Latham[48], C. Lazzeroni[45], R. Le Gac[6], J. van Leerdam[41], J.-P. Lees[4], R. Lefèvre[5], A. Leflat[32], J. Lefrançois[7], S. Leo[23], O. Leroy[6], T. Lesiak[26], B. Leverington[11], Y. Li[3], T. Likhomanenko[63], M. Liles[52], R. Lindner[38], C. Linn[38], F. Lionetto[40], B. Liu[15], S. Lohn[38], I. Longstaff[51], J.H. Lopes[2], N. Lopez-March[39], P. Lowdon[40], H. Lu[3], D. Lucchesi[22,r], H. Luo[50], A. Lupato[22], E. Luppi[16,f], O. Lupton[55], F. Machefert[7], I.V. Machikhiliyan[31], F. Maciuc[29], O. Maev[30], S. Malde[55], A. Malinin[63], G. Manca[15,e], G. Mancinelli[6], A. Mapelli[38], J. Maratas[5], J.F. Marchand[4], U. Marconi[14], C. Marin Benito[36], P. Marino[23,t], R. Märki[39], J. Marks[11], G. Martellotti[25], A. Martens[8], A. Martín Sánchez[7], M. Martinelli[39], D. Martinez Santos[42], F. Martinez Vidal[64], D. Martins Tostes[2], A. Massafferri[1], R. Matev[38], Z. Mathe[38], C. Matteuzzi[20], A. Mazurov[16,f], M. McCann[53], J. McCarthy[45], A. McNab[54], R. McNulty[12], B. McSkelly[52], B. Meadows[57], F. Meier[9], M. Meissner[11], M. Merk[41], D.A. Milanes[8], M.-N. Minard[4], N. Moggi[14], J. Molina Rodriguez[60], S. Monteil[5], M. Morandin[22], P. Morawski[27], A. Mordà[6], M.J. Morello[23,t], J. Moron[27], A.-B. Morris[50], R. Mountain[59], F. Muheim[50], K. Müller[40], M. Mussini[14], B. Muster[39], P. Naik[46], T. Nakada[39], R. Nandakumar[49], I. Nasteva[2], M. Needham[50], N. Neri[21], S. Neubert[38], N. Neufeld[38], M. Neuner[11], A.D. Nguyen[39], T.D. Nguyen[39], C. Nguyen-Mau[39,q], M. Nicol[7], V. Niess[5], R. Niet[9], N. Nikitin[32], T. Nikodem[11], A. Novoselov[35], D.P. O'Hanlon[48], A. Oblakowska-Mucha[27], V. Obraztsov[35], S. Oggero[41], S. Ogilvy[51], O. Okhrimenko[44], R. Oldeman[15,e], G. Onderwater[65], M. Orlandea[29], J.M. Otalora Goicochea[2], P. Owen[53], A. Oyanguren[64], B.K. Pal[59], A. Palano[13,c], F. Palombo[21,u], M. Palutan[18], J. Panman[38], A. Papanestis[49,38], M. Pappagallo[51], L.L. Pappalardo[16,f], C. Parkes[54], C.J. Parkinson[9,45], G. Passaleva[17], G.D. Patel[52], M. Patel[53], C. Patrignani[19,j], A. Pazos Alvarez[37], A. Pearce[54], A. Pellegrino[41], M. Pepe Altarelli[38], S. Perazzini[14,d], E. Perez Trigo[37], P. Perret[5], M. Perrin-Terrin[6], L. Pescatore[45], E. Pesen[66], K. Petridis[53], A. Petrolini[19,j], E. Picatoste Olloqui[36], B. Pietrzyk[4], T. Pilař[48], D. Pinci[25], A. Pistone[19], S. Playfer[50], M. Plo Casasus[37], F. Polci[8], A. Poluektov[48,34], E. Polycarpo[2], A. Popov[35], D. Popov[10], B. Popovici[29], C. Potterat[2], E. Price[46], J. Prisciandaro[39], A. Pritchard[52], C. Prouve[46], V. Pugatch[44], A. Puig Navarro[39], G. Punzi[23,s], W. Qian[4], B. Rachwal[26], J.H. Rademacker[46], B. Rakotomiaramanana[39], M. Rama[18], M.S. Rangel[2], I. Raniuk[43], N. Rauschmayr[38], G. Raven[42], S. Reichert[54], M.M. Reid[48], A.C. dos Reis[1], S. Ricciardi[49], S. Richards[46], M. Rihl[38], K. Rinnert[52], V. Rives Molina[36], D.A. Roa Romero[5], P. Robbe[7], A.B. Rodrigues[1], E. Rodrigues[54], P. Rodriguez Perez[54], S. Roiser[38], V. Romanovsky[35], A. Romero Vidal[37], M. Rotondo[22], J. Rouvinet[39], T. Ruf[38], H. Ruiz[36], P. Ruiz Valls[64], J.J. Saborido Silva[37], N. Sagidova[30], P. Sail[51], B. Saitta[15,e], V. Salustino Guimaraes[2], C. Sanchez Mayordomo[64],

B. Sanmartin Sedes[37], R. Santacesaria[25], C. Santamarina Rios[37], E. Santovetti[24,l], A. Sarti[18,m], C. Satriano[25,n], A. Satta[24], D.M. Saunders[46], M. Savrie[16,f], D. Savrina[31,32], M. Schiller[42], H. Schindler[38], M. Schlupp[9], M. Schmelling[10], B. Schmidt[38], O. Schneider[39], A. Schopper[38], M.-H. Schune[7], R. Schwemmer[38], B. Sciascia[18], A. Sciubba[25], M. Seco[37], A. Semennikov[31], I. Sepp[53], N. Serra[40], J. Serrano[6], L. Sestini[22], P. Seyfert[11], M. Shapkin[35], I. Shapoval[16,43,f], Y. Shcheglov[30], T. Shears[52], L. Shekhtman[34], V. Shevchenko[63], A. Shires[9], R. Silva Coutinho[48], G. Simi[22], M. Sirendi[47], N. Skidmore[46], T. Skwarnicki[59], N.A. Smith[52], E. Smith[55,49], E. Smith[53], J. Smith[47], M. Smith[54], H. Snoek[41], M.D. Sokoloff[57], F.J.P. Soler[51], F. Soomro[39], D. Souza[46], B. Souza De Paula[2], B. Spaan[9], A. Sparkes[50], P. Spradlin[51], S. Sridharan[38], F. Stagni[38], M. Stahl[11], S. Stahl[11], O. Steinkamp[40], O. Stenyakin[35], S. Stevenson[55], S. Stoica[29], S. Stone[59], B. Storaci[40], S. Stracka[23,38], M. Straticiuc[29], U. Straumann[40], R. Stroili[22], V.K. Subbiah[38], L. Sun[57], W. Sutcliffe[53], K. Swientek[27], S. Swientek[9], V. Syropoulos[42], M. Szczekowski[28], P. Szczypka[39,38], D. Szilard[2], T. Szumlak[27], S. T'Jampens[4], M. Teklishyn[7], G. Tellarini[16,f], F. Teubert[38], C. Thomas[55], E. Thomas[38], J. van Tilburg[41], V. Tisserand[4], M. Tobin[39], S. Tolk[42], L. Tomassetti[16,f], D. Tonelli[38], S. Topp-Joergensen[55], N. Torr[55], E. Tournefier[4], S. Tourneur[39], M.T. Tran[39], M. Tresch[40], A. Tsaregorodtsev[6], P. Tsopelas[41], N. Tuning[41], M. Ubeda Garcia[38], A. Ukleja[28], A. Ustyuzhanin[63], U. Uwer[11], V. Vagnoni[14], G. Valenti[14], A. Vallier[7], R. Vazquez Gomez[18], P. Vazquez Regueiro[37], C. Vázquez Sierra[37], S. Vecchi[16], J.J. Velthuis[46], M. Veltri[17,h], G. Veneziano[39], M. Vesterinen[11], B. Viaud[7], D. Vieira[2], M. Vieites Diaz[37], X. Vilasis-Cardona[36,p], A. Vollhardt[40], D. Volyanskyy[10], D. Voong[46], A. Vorobyev[30], V. Vorobyev[34], C. Voß[62], H. Voss[10], J.A. de Vries[41], R. Waldi[62], C. Wallace[48], R. Wallace[12], J. Walsh[23], S. Wandernoth[11], J. Wang[59], D.R. Ward[47], N.K. Watson[45], D. Websdale[53], M. Whitehead[48], J. Wicht[38], D. Wiedner[11], G. Wilkinson[55], M.P. Williams[45], M. Williams[56], F.F. Wilson[49], J. Wimberley[58], J. Wishahi[9], W. Wislicki[28], M. Witek[26], G. Wormser[7], S.A. Wotton[47], S. Wright[47], S. Wu[3], K. Wyllie[38], Y. Xie[61], Z. Xing[59], Z. Xu[39], Z. Yang[3], X. Yuan[3], O. Yushchenko[35], M. Zangoli[14], M. Zavertyaev[10,b], L. Zhang[59], W.C. Zhang[12], Y. Zhang[3], A. Zhelezov[11], A. Zhokhov[31], L. Zhong[3], A. Zvyagin[38].

[1] *Centro Brasileiro de Pesquisas Físicas (CBPF), Rio de Janeiro, Brazil*
[2] *Universidade Federal do Rio de Janeiro (UFRJ), Rio de Janeiro, Brazil*
[3] *Center for High Energy Physics, Tsinghua University, Beijing, China*
[4] *LAPP, Université de Savoie, CNRS/IN2P3, Annecy-Le-Vieux, France*
[5] *Clermont Université, Université Blaise Pascal, CNRS/IN2P3, LPC, Clermont-Ferrand, France*
[6] *CPPM, Aix-Marseille Université, CNRS/IN2P3, Marseille, France*
[7] *LAL, Université Paris-Sud, CNRS/IN2P3, Orsay, France*
[8] *LPNHE, Université Pierre et Marie Curie, Université Paris Diderot, CNRS/IN2P3, Paris, France*
[9] *Fakultät Physik, Technische Universität Dortmund, Dortmund, Germany*
[10] *Max-Planck-Institut für Kernphysik (MPIK), Heidelberg, Germany*
[11] *Physikalisches Institut, Ruprecht-Karls-Universität Heidelberg, Heidelberg, Germany*
[12] *School of Physics, University College Dublin, Dublin, Ireland*
[13] *Sezione INFN di Bari, Bari, Italy*
[14] *Sezione INFN di Bologna, Bologna, Italy*
[15] *Sezione INFN di Cagliari, Cagliari, Italy*
[16] *Sezione INFN di Ferrara, Ferrara, Italy*
[17] *Sezione INFN di Firenze, Firenze, Italy*
[18] *Laboratori Nazionali dell'INFN di Frascati, Frascati, Italy*
[19] *Sezione INFN di Genova, Genova, Italy*
[20] *Sezione INFN di Milano Bicocca, Milano, Italy*
[21] *Sezione INFN di Milano, Milano, Italy*

[22] *Sezione INFN di Padova, Padova, Italy*
[23] *Sezione INFN di Pisa, Pisa, Italy*
[24] *Sezione INFN di Roma Tor Vergata, Roma, Italy*
[25] *Sezione INFN di Roma La Sapienza, Roma, Italy*
[26] *Henryk Niewodniczanski Institute of Nuclear Physics Polish Academy of Sciences, Kraków, Poland*
[27] *AGH - University of Science and Technology, Faculty of Physics and Applied Computer Science, Kraków, Poland*
[28] *National Center for Nuclear Research (NCBJ), Warsaw, Poland*
[29] *Horia Hulubei National Institute of Physics and Nuclear Engineering, Bucharest-Magurele, Romania*
[30] *Petersburg Nuclear Physics Institute (PNPI), Gatchina, Russia*
[31] *Institute of Theoretical and Experimental Physics (ITEP), Moscow, Russia*
[32] *Institute of Nuclear Physics, Moscow State University (SINP MSU), Moscow, Russia*
[33] *Institute for Nuclear Research of the Russian Academy of Sciences (INR RAN), Moscow, Russia*
[34] *Budker Institute of Nuclear Physics (SB RAS) and Novosibirsk State University, Novosibirsk, Russia*
[35] *Institute for High Energy Physics (IHEP), Protvino, Russia*
[36] *Universitat de Barcelona, Barcelona, Spain*
[37] *Universidad de Santiago de Compostela, Santiago de Compostela, Spain*
[38] *European Organization for Nuclear Research (CERN), Geneva, Switzerland*
[39] *Ecole Polytechnique Fédérale de Lausanne (EPFL), Lausanne, Switzerland*
[40] *Physik-Institut, Universität Zürich, Zürich, Switzerland*
[41] *Nikhef National Institute for Subatomic Physics, Amsterdam, The Netherlands*
[42] *Nikhef National Institute for Subatomic Physics and VU University Amsterdam, Amsterdam, The Netherlands*
[43] *NSC Kharkiv Institute of Physics and Technology (NSC KIPT), Kharkiv, Ukraine*
[44] *Institute for Nuclear Research of the National Academy of Sciences (KINR), Kyiv, Ukraine*
[45] *University of Birmingham, Birmingham, United Kingdom*
[46] *H.H. Wills Physics Laboratory, University of Bristol, Bristol, United Kingdom*
[47] *Cavendish Laboratory, University of Cambridge, Cambridge, United Kingdom*
[48] *Department of Physics, University of Warwick, Coventry, United Kingdom*
[49] *STFC Rutherford Appleton Laboratory, Didcot, United Kingdom*
[50] *School of Physics and Astronomy, University of Edinburgh, Edinburgh, United Kingdom*
[51] *School of Physics and Astronomy, University of Glasgow, Glasgow, United Kingdom*
[52] *Oliver Lodge Laboratory, University of Liverpool, Liverpool, United Kingdom*
[53] *Imperial College London, London, United Kingdom*
[54] *School of Physics and Astronomy, University of Manchester, Manchester, United Kingdom*
[55] *Department of Physics, University of Oxford, Oxford, United Kingdom*
[56] *Massachusetts Institute of Technology, Cambridge, MA, United States*
[57] *University of Cincinnati, Cincinnati, OH, United States*
[58] *University of Maryland, College Park, MD, United States*
[59] *Syracuse University, Syracuse, NY, United States*
[60] *Pontifícia Universidade Católica do Rio de Janeiro (PUC-Rio), Rio de Janeiro, Brazil, associated to* [2]
[61] *Institute of Particle Physics, Central China Normal University, Wuhan, Hubei, China, associated to* [3]
[62] *Institut für Physik, Universität Rostock, Rostock, Germany, associated to* [11]
[63] *National Research Centre Kurchatov Institute, Moscow, Russia, associated to* [31]
[64] *Instituto de Fisica Corpuscular (IFIC), Universitat de Valencia-CSIC, Valencia, Spain, associated to* [36]
[65] *KVI - University of Groningen, Groningen, The Netherlands, associated to* [41]
[66] *Celal Bayar University, Manisa, Turkey, associated to* [38]

[a] *Universidade Federal do Triângulo Mineiro (UFTM), Uberaba-MG, Brazil*
[b] *P.N. Lebedev Physical Institute, Russian Academy of Science (LPI RAS), Moscow, Russia*
[c] *Università di Bari, Bari, Italy*
[d] *Università di Bologna, Bologna, Italy*

[e] *Università di Cagliari, Cagliari, Italy*
[f] *Università di Ferrara, Ferrara, Italy*
[g] *Università di Firenze, Firenze, Italy*
[h] *Università di Urbino, Urbino, Italy*
[i] *Università di Modena e Reggio Emilia, Modena, Italy*
[j] *Università di Genova, Genova, Italy*
[k] *Università di Milano Bicocca, Milano, Italy*
[l] *Università di Roma Tor Vergata, Roma, Italy*
[m] *Università di Roma La Sapienza, Roma, Italy*
[n] *Università della Basilicata, Potenza, Italy*
[o] *AGH - University of Science and Technology, Faculty of Computer Science, Electronics and Telecommunications, Kraków, Poland*
[p] *LIFAELS, La Salle, Universitat Ramon Llull, Barcelona, Spain*
[q] *Hanoi University of Science, Hanoi, Viet Nam*
[r] *Università di Padova, Padova, Italy*
[s] *Università di Pisa, Pisa, Italy*
[t] *Scuola Normale Superiore, Pisa, Italy*
[u] *Università degli Studi di Milano, Milano, Italy*
[v] *Politecnico di Milano, Milano, Italy*